

Improved multi-body rope approach for free-form gridshell structures using equal-length element strategy

*Original*

Improved multi-body rope approach for free-form gridshell structures using equal-length element strategy / Manuello Bertetto, Amedeo; Melchiorre, Jonathan; Marano, Giuseppe Carlo. - In: AUTOMATION IN CONSTRUCTION. - ISSN 0926-5805. - 161:(2024), pp. 1-22. [10.1016/j.autcon.2024.105340]

*Availability:*

This version is available at: 11583/2986944 since: 2024-03-13T10:31:25Z

*Publisher:*

Elsevier

*Published*

DOI:10.1016/j.autcon.2024.105340

*Terms of use:*

This article is made available under terms and conditions as specified in the corresponding bibliographic description in the repository

*Publisher copyright*

Elsevier postprint/Author's Accepted Manuscript

© 2024. This manuscript version is made available under the CC-BY-NC-ND 4.0 license  
<http://creativecommons.org/licenses/by-nc-nd/4.0/>. The final authenticated version is available online at:  
<http://dx.doi.org/10.1016/j.autcon.2024.105340>

(Article begins on next page)

1 Improved Multi-body Rope Approach for Free-Form  
2 Gridshell Structures Using Equal-Length Element  
3 Strategy

4 Amedeo Manuello Bertetto<sup>a</sup>, Jonathan Melchiorre<sup>a,\*</sup>, Giuseppe Carlo  
5 Marano<sup>a,b</sup>

<sup>a</sup>*Politecnico di Torino, DISEG, Department of Structural, Geotechnical and Building  
Engineering, Corso Duca Degli Abruzzi, 24, Turin, 10129, Italy*

<sup>b</sup>*Fuzhou University, College of Civil Engineering, Xueyuan Rd, Gulou  
District, Fuzhou, 350025, China*

---

6 **Abstract**

7 Gridshell roofing constructions are favoured in modern engineering and architecture for  
8 their capacity to produce expansive, lightweight roofs using slender main structural ele-  
9 ments, yet their complex and costly fabrication limits broader adoption. The Multi-body  
10 Rope Approach (MRA) is effective in computing structurally efficient geometries in grid-  
11 shells, emphasizing the need to optimize design configurations for minimal internal stresses.  
12 This paper presents two strategies, Multiple Order MRA (MO-MRA) and Repulsive Nodes  
13 MRA (RN-MRA), to improve the MRA and streamline gridshell construction by reduc-  
14 ing the necessary types of structural components. These approaches are combined in an  
15 improved MRA (i-MRA), reducing manufacturing costs and increasing efficiency in con-  
16 struction management. The i-MRA was implemented in Matlab and tested on four case  
17 studies of increasing complexity, demonstrating its effectiveness.

18 *Keywords:* Form finding, Gridshell, Structural Optimization, Construction  
19 Process, Structural engineering

---

20 **1. Introduction**

21 In recent years, there has been a growing demand for architectural struc-  
22 tures that offer greater internal distribution flexibility and allow for free-form

23 designs in big-span roofing projects. Double-curved shells and domes have  
24 emerged as a feasible alternative for achieving at the same time column-free  
25 spaces and complex shapes [1]. Free-form shell structures, also known as  
26 curved shell structures, have gained significant attention due to their unique  
27 and aesthetically pleasing qualities [2]. These structures feature complex,  
28 curved shapes that challenge traditional construction methods and require  
29 innovative design and engineering solutions.

30 Free-form shell structures are widely used in the construction of large-  
31 scale buildings. Shells are self-supporting thin structures with single or dou-  
32 ble curvature that can cover broad-span areas without the need for beams,  
33 columns, or walls. Their curved shape provides an ideal morphology for vari-  
34 ous load patterns and multiple stress paths, making them highly efficient. In  
35 shell constructions, membrane actions are primarily related to plane stress,  
36 while bending deformation can result in secondary forces. The most desirable  
37 behaviour for shells is the membranous one, as it exhibits higher structural  
38 efficiency. However, if compressive membrane states are present, sufficient  
39 bending stiffness must be provided to prevent local (buckling) and non-local  
40 (snap-through) instability problems.

41 A gridshell is a type of free-form shell structure that comprises a three-  
42 dimensional grid of linear elements interconnected by nodes. This unique  
43 structure exhibits the mechanical behaviour of shells and combines the soft  
44 curves of shell structures with the rigidity and strength of structural grids.  
45 As a result, gridshells offer a range of structural and aesthetic benefits. They  
46 are lightweight, self-supporting structures that can span large areas while  
47 minimizing material usage. Recent studies have demonstrated the potential

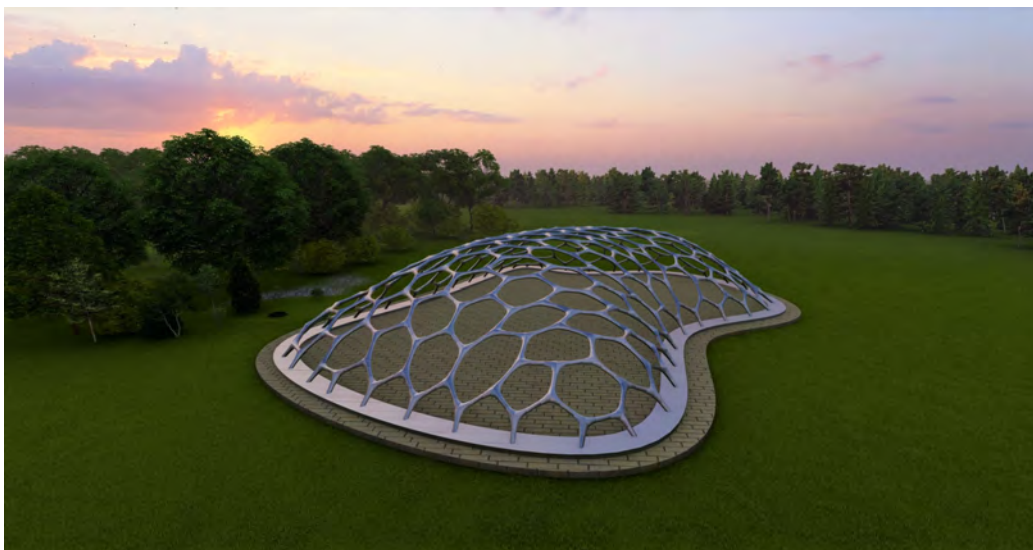


Figure 1: Free-form gridshell structure generated with Multi-body Rope Approach.

48 of gridshells for structural applications, including in the fields of architecture,  
49 engineering, and design [3, 4].

50 Gridshell structures have a rich history dating back to the mid-20th cen-  
51 tury, when architects and engineers began to experiment with innovative  
52 materials and structural systems. Among the earliest examples of gridshell  
53 design was the Zeiss Planetarium in Jena, Germany, completed in 1923, fea-  
54 turing a dome made of thin, curved wood panels.

55 In the 1960s and 70s, architects and engineers like Frei Otto [5] and Ted  
56 Happold [6, 7] pioneered new approaches to gridshell design. They used  
57 lightweight materials and computer modelling to create complex, double-  
58 curved forms. Early gridshells were commonly built with materials such as  
59 timber [8] or fabric and were used to create vast open spaces like exhibition  
60 halls, sports arenas [9], and airport terminals.

61 In recent decades, advances in digital design and fabrication technologies

62 have allowed architects and engineers to push the boundaries of gridshell  
63 design even further. Gridshell structures are now commonly made from ma-  
64 terials such as steel [10, 11], aluminium [12], wood [13, 14, 15, 16], and elastic  
65 composite materials [17, 18, 19].

66 Despite their many advantages, the construction of gridshell structures  
67 remains limited due to the complexity of their geometry and structural chal-  
68 lenges [20]. In addition, the need for expensive assembly technologies and  
69 precise form-finding to ensure stability has made the design and construction  
70 of gridshells a challenging task.

71 Moreover, the lack of data on this structural typology has hindered its  
72 wider adoption in the industry [21]. However, recent advancements in com-  
73 puting systems have greatly improved the ability to analyze increasingly com-  
74 plex systems, making gridshell architecture an increasingly viable option [22].  
75 As a result, continued growth in the use of gridshells in the design and con-  
76 struction of large, open structures can be expected in the years to come.

77 Gridshell structures are defined by the interaction between their shape  
78 and stress distribution. Because of this relationship between shape and  
79 forces, designing such structures directly, as in the case of conventional struc-  
80 tures, is ineffective. In this scenario, the search for a suitable structural shape  
81 is critical, both for design aesthetics and, more importantly, for the struc-  
82 ture’s capability to support loads. To achieve a feasible shape, it is necessary  
83 to balance the internal forces and loads acting on the structure and minimize  
84 the bending moment within the resisting elements [23]. Form-finding is a vi-  
85 tal step in designing free-form gridshell structures, where the optimal shape  
86 and layout of the structural elements are determined under a specific load

87 pattern. Various form-finding methods have been developed over the years to  
88 facilitate the design of these complex structures, including both physical and  
89 computational modelling techniques [24]. Among the most popular form-  
90 finding methods are the force density method [25], thrust network analysis  
91 [26], dynamic relaxation method [27], particle-spring system [28], multi-body  
92 rope approach [29], and others [30, 31, 32].

93 The primary objective of these techniques is to identify a structural shape  
94 that meets the boundary requirements, reduces the cost of construction, and  
95 has an aesthetically pleasing appearance. The cutting-edge trend in struc-  
96 tural design research involves coupling innovative shapes and free-form struc-  
97 tures with structural optimization [33, 34, 35]. A significant challenge lies in  
98 defining a structural model that is optimized not only structurally but also  
99 geometrically and constructively. Additionally, optimizing the production of  
100 the structural elements and managing the construction stages poses a final  
101 challenge in form-finding and optimization.

102 To overcome these challenges, architects and engineers have developed  
103 several techniques and tools to optimize the design of structural elements,  
104 panelling patterns [36, 37], and nodes [38, 39] in gridshells. These may in-  
105 clude digital simulations and models, advanced material analysis techniques,  
106 and the use of parametric design tools to explore and refine different design  
107 options.

108 This paper presents an original development for the form-finding method  
109 developed specifically for gridshells: the improved Multi-body Rope Ap-  
110 proach (i-MRA). The i-MRA method builds on the Multi-body Rope Ap-  
111 proach (MRA) [29], a form-finding technique used in structural engineering

112 for designing complex shell and gridshell structures.

113 In MRA, a structure is represented as a network of masses connected by  
114 flexible ropes or cables. This allows for the definition of the geometry of  
115 the structure by minimizing bending moments and stresses [40]. The MRA  
116 approach defines the structural geometry by minimizing the eccentricity of  
117 applied compression forces [41].

118 The i-MRA method improves on MRA by integrating techniques that  
119 optimize the structural geometry for both structural reasons and automation  
120 of the construction process. There are two main improvements to i-MRA:

- 121 • Multiple Orders MRA (MO-MRA): groups structural elements with  
122 identical lengths, reducing the number of types of structural compo-  
123 nents required for construction.
- 124 • Repulsive Nodes MRA (RN-MRA): applies a repulsive force field to the  
125 dynamic model, which allows for minor adjustments to the geometry  
126 to reduce the number of structural components required.

127 Implemented in MATLAB, i-MRA provides a powerful tool for generating  
128 optimal structural geometries with minimal bending moments and stress. It  
129 also reduces the types of structural components required for construction,  
130 leading to lower production costs, encouraging mass production, and reducing  
131 expenses related to construction management.

132 The i-MRA method has been tested on four examples of increasing com-  
133 plexity, demonstrating its effectiveness in generating optimal structural ge-  
134 ometries.

135 To verify that the geometries obtained by the proposed new method  
136 did not have significant structural disadvantages (in terms of internal so-  
137 licitations) compared with those calculated by pure form-finding methods,  
138 a structural analysis of the structures obtained by basic MRA and i-MRA  
139 was carried out. For this purpose, finite element analyses were conducted  
140 using SOFiSTiK software [42]. Axial force, bending moment, and Von Mises  
141 stresses acting on the two structural geometries were compared by imposing  
142 a unit load of -1 kN in the vertical direction on each unrestrained structural  
143 node. The study assumed that CHS 200 5 profiles and S275 structural steel  
144 were used.

145 The comparison was made in terms of axial force since the structural type  
146 studied is mainly subject to this type of internal action. The comparison in  
147 terms of bending moment was chosen because form-finding methods typi-  
148 cally aim to minimize the bending moment acting on structures. Therefore,  
149 it was important to demonstrate that small deviations from the geometry  
150 obtained by pure form-finding did not produce significant increases in the  
151 acting bending moment.

152 The paper is organized as follows. In section 2 the basic equation of the  
153 MRA method and the i-MRA are introduced. In particular, in sections 2.1  
154 and 2.2 the techniques for the improvement of the MRA method are pre-  
155 sented. Then, in section 3 the results of the application of the new method  
156 on different case-studies in terms of obtained geometries and structural anal-  
157 yses are reported. Finally, section 4 is focused on the conclusions and some  
158 possible future developments of the presented research topic.

## 159 2. Methodology

160 The Multibody Rope Approach (MRA), developed by [29], is an origi-  
161 nal method for determining the form of gridshell structures, even for highly  
162 complex geometries and for any type of forming load. It is specifically de-  
163 signed for gridshell constructions that use free-forms and standardized build-  
164 ing elements. MRA utilizes a dynamic model of falling bodies in space and  
165 time domains, in which the final equilibrium configuration is calculated iter-  
166 atively for each node using the D’Alembert’s principle. The special feature  
167 of the method is to consider structural elements as ropes connecting masses  
168 to nodes. The aim of this approach is to generate a geometry that is both  
169 structurally optimal and composed of the greatest possible number of parts  
170 of identical length. The final equilibrium configuration of the structure is  
171 an inverted representation of the hanging net (funicular configuration). Like  
172 particle-spring models, MRA assumes that the self-weight of the nodes and  
173 the load of the ropes are localized at the nodes. However, MRA differs from  
174 these approaches in its use of ropes to model the hanging network. The  
175 ropes have a specific slack coefficient that allows for regular forms. In MRA,  
176 the system of forces acting on individual nodes is distinct from those in the  
177 spring-particle (SP) and dynamic relaxation (DR) methods. Specifically, the  
178 rope element exerts forces on the masses so that they do not move apart be-  
179 yond the prescribed distance, which is precisely the length of the rope. When  
180 the distance between the ends is smaller than the predetermined length of  
181 the rope ( $l_{rope}$ ), no force is applied. By defining  $l$  as the distance between  
182 the two ends of the rope and  $k$  as the axial stiffness of the rope, the forces  
183  $F$  applied to the end nodes can be expressed as follows:

$$\begin{cases} F_{rope} = 0 & \text{if } l < l_{rope} \\ F_{rope} = k(l - l_{rope}) & \text{if } l \geq l_{rope} \end{cases} \quad (1)$$

184 Where the length of the rope  $l_{ji}$  between the two nodes  $i$  and  $j$  can be  
 185 calculated as:

$$l_{ji} = \sqrt{(x_j - x_i)^2 + (y_j - y_i)^2 + (z_j - z_i)^2} \quad (2)$$

186 In general, the MRA approach aims to minimize axial deformations by  
 187 assuming extremely high stiffness values. The goal of MRA is to find a  
 188 geometric configuration that ensures the equilibrium of nodes subjected to  
 189 external forces and those emerging from the ropes connected to them. Let's  
 190 consider a generic node  $i$  with a mass of  $m_i$  in the structural network of  
 191 nodes and ropes. The node  $i$  is connected to a number  $n_i$  of other nodes  
 192 through ropes. If there is an external load  $p_i$  acting on node  $i$ , the equilibrium  
 193 equation can be written as:

$$\vec{R}_i = \vec{p}_i + \sum_{j=1}^{n_i} \vec{F}_{rope,ji} + \vec{F}_i^I + \vec{F}_i^{II} = 0 \quad (3)$$

194 In this equation, the vector  $\vec{R}_i$  represents the net force acting on node  $i$ ,  
 195 which is the sum of several forces including the applied load  $p_i$ , the forces  
 196 transmitted by the ropes connected to the node  $\vec{F}_{rope,ji}$ , the inertial force  
 197  $\vec{F}_i^{II}$ , and the damping force  $\vec{F}_i^I$ . The magnitude of the inertial force  $\vec{F}_i^{II}$   
 198 can be determined using equation (4), which is calculated as the product of  
 199 the node's mass  $m_i$  and the magnitude of the acceleration vector  $\vec{a}_i$ , with  
 200 the direction of the inertial force being opposite to the direction of node

201 acceleration.

$$\vec{F}_i^{II} = -m_i \cdot \vec{a}_i \quad (4)$$

202 The damping force  $\vec{F}_i^I$  is represented by the product of a constant damp-  
 203 ing coefficient  $c_i$  and the velocity vector  $\vec{v}_i$  with direction opposite to the  
 204 direction of the velocity. This relationship is expressed in equation (5).

$$\vec{F}_i^I = -c_i \cdot \vec{v}_i \quad (5)$$

205 Expressing the position of the generic node  $i$  as  $\vec{u}_i = (x_i, y_i, z_i)$ , the  
 206 velocity and the acceleration can be obtained by deriving the position in  
 207 time, as in the relations (6).

$$\vec{v}_i = \dot{\vec{u}}_i = (\dot{x}_i, \dot{y}_i, \dot{z}_i) \quad \vec{a}_i = \ddot{\vec{u}}_i = (\ddot{x}_i, \ddot{y}_i, \ddot{z}_i) \quad (6)$$

208 Thus, the equation (3) can be rewritten as in (7).

$$\vec{R}_i = \vec{p}_i + \sum_{j=1}^{n_i} \left\{ k \cdot \vec{F}_{rope,ji} \right\} - c_i \cdot \vec{v}_i - m_i \cdot \vec{a}_i = 0 \quad (7)$$

209 Finally, the equilibrium equation (7) can be projected in the three space  
 210 dimensions, obtaining the system of equation (8).

$$\begin{cases} p_{ix} + \sum_{j=1}^{n_i} \left\{ \frac{(x_j - x_i)}{l_{ji}} \cdot F_{rope} \right\} - c_i \cdot \dot{x}_i - m_i \cdot \ddot{x}_i = 0 \\ p_{iy} + \sum_{j=1}^{n_i} \left\{ \frac{(y_j - y_i)}{l_{ji}} \cdot F_{rope} \right\} - c_i \cdot \dot{y}_i - m_i \cdot \ddot{y}_i = 0 \\ p_{iz} + \sum_{j=1}^{n_i} \left\{ \frac{(z_j - z_i)}{l_{ji}} \cdot F_{rope} \right\} - c_i \cdot \dot{z}_i - m_i \cdot \ddot{z}_i = 0 \end{cases} \quad (8)$$

211 The system of equations can be solved by considering a time increment  
 212 of  $\Delta t$ . The positions of the nodes at time  $t = 0$  are assumed to be known,

213 and initial velocities and accelerations are assumed to be zero for each node  $i$   
 214 ( $v_i(0) = 0$  and  $a_i(0) = 0$ ). By knowing the position, velocity, and acceleration  
 215 of each node at time  $t$ , these quantities can be determined at the next instant,  
 216  $t + \Delta t$ . To do so, a coefficient  $C_3$  can be defined as a function of the known  
 217 node positions at time  $t^*$ , as shown in equation (9).

$$C_3 = \vec{p}_i + \sum_{j=1}^{n_i} \left\{ k \cdot \vec{F}_{rope,ji} \right\} \quad (9)$$

218 The coefficient  $C_3$  depends solely on the position of the nodes at time  $t^*$ ,  
 219 and it defines the vector  $F_{rope}$ . Consequently, Equation (7) can be reformu-  
 220 lated as shown in (10).

$$\ddot{\vec{u}} + \frac{c}{m} \dot{\vec{u}} = C_3 \quad (10)$$

221 In addition, the natural frequency of the system  $\omega_n$  and critical damping  
 222  $\zeta$  can be defined as in the equations (11) and (12).

$$\omega_n = \sqrt{\frac{k}{m}} \quad (11)$$

$$\zeta = \frac{c}{2\omega_n m} \quad (12)$$

223 where  $k$  is the stiffness,  $m$  is the mass, and  $c$  is the damping coefficient  
 224 of the system. The natural frequency  $\omega_n$  represents the frequency at which  
 225 the system vibrates when it is not subjected to any external forces. The  
 226 critical damping  $\zeta$  is the damping coefficient value that results in the system  
 227 being critically damped, which means that it returns to its equilibrium state

228 as quickly as possible without oscillating. Thus, a non-homogeneous second-  
 229 order differential equation is obtained:

$$\ddot{\vec{u}} + 2\omega_n\zeta\dot{\vec{u}} = C_3 \quad (13)$$

230 The solution to the equation (13) can be obtained by adding the partic-  
 231 ular solution to the associated homogeneous differential equation, which is  
 232 expressed as (14).

$$\vec{u}(t) = C_1 e^{-2\omega_n\zeta t} + C_2 + \frac{C_3}{2\omega_n\zeta} t \quad (14)$$

233 The coefficients  $C_1$  and  $C_2$  can be calculated based on the initial condi-  
 234 tions of the system. In this case, they can be obtained by using the positions  
 235 and velocities of the nodes at the immediately preceding instant  $t - \Delta t$ , as  
 236 shown in the following equations:

$$C_1 = -\frac{2\omega_n\zeta\dot{\vec{u}}_{(t-\Delta t)} - C_3}{(2\omega_n\zeta)^2} \quad (15)$$

$$C_2 = -\frac{(2\omega_n\zeta)^2\vec{u}_{(t-\Delta t)} + 2\omega_n\zeta\dot{\vec{u}}_{(t-\Delta t)} - C_3}{(2\omega_n\zeta)^2} \quad (16)$$

237 The coefficients  $C_1$ ,  $C_2$ , and  $C_3$  in the solution depend on the positions,  
 238 velocities, and accelerations of the system's nodes at the previous time in-  
 239 stant. Starting from the initial state where the location of the nodes in the  
 240 three-dimensional space is known and velocity and acceleration are zero, the  
 241 positions of the nodes at succeeding instants can be calculated progressively.  
 242 The velocity vector  $\dot{\vec{u}}_t$  can be obtained by taking the difference between the  
 243 positions of the nodes at instants  $t - \Delta t$  and  $t$ , and dividing by the time  
 244 increment  $\Delta t$ :

$$\dot{\vec{u}}_t = \frac{\vec{u}_t - \vec{u}_{t-\Delta t}}{\Delta t} \quad (17)$$

245 Finally, the acceleration  $\ddot{\vec{u}}_t$  can be determined by computing the ratio of  
 246 the incremental change in velocity between two time instants  $t - \Delta t$  and  $t$ .  
 247 Specifically, this can be achieved by calculating the difference between the  
 248 two velocities and dividing it by the time interval  $\Delta t$ .

$$\ddot{\vec{u}}_t = \frac{\dot{\vec{u}}_t - \dot{\vec{u}}_{t-\Delta t}}{\Delta t} \quad (18)$$

249 The proposed method is designed to calculate the final configuration of  
 250 a gridshell from its initial mesh, which represents the initial state of the  
 251 net. Since the initial position of nodes is known, and their initial velocities  
 252 and accelerations are assumed to be zero, the new locations, velocities, and  
 253 accelerations of nodes can be determined sequentially using equations (14),  
 254 (17), and (18). This process is repeated until an equilibrium configuration  
 255 is reached that represents the optimal structural geometry with respect to  
 256 the applied force field  $\vec{p}$ . The estimated structural geometry is a function  
 257 of various parameters, including the nodal masses  $m$ , the system stiffness  
 258  $k$ , damping parameters  $c$ , the rope slack coefficient  $\rho$ , and the applied force  
 259 field  $\vec{p}$ . The slack coefficient  $\rho$  is defined as the ratio of the initial distance  
 260 between nodes to the target length of the ropes, as shown in equation (19).

$$\rho_{ij} = \frac{l_{rope}}{|\vec{u}_i(0) - \vec{u}_j(0)|} = \frac{l_{rope}}{\sqrt{(x_i - x_j)^2 + (y_i - y_j)^2 + (z_i - z_j)^2}} \quad (19)$$

261 The objective of applying MRA is to generate a structural geometry that  
 262 is optimal in terms of both structural effectiveness and ease of construction.

263 To evaluate the ease of construction, the number of beam elements of equal  
264 length is used as a measure. In practice, the complexity of gridshell assembly  
265 increases exponentially as the number of different elements to be assembled  
266 grows. Therefore, it is crucial to determine the number of elements in the  
267 final configuration that have a length equal to the target length  $l_{rope}$ , while  
268 considering a certain tolerance  $toll$ . Based on their length, structural ele-  
269 ments are classified into three categories: those with a length less than  $l_{rope}$   
270 are called *loose elements*, those with a length greater than  $l_{rope}$  are called  
271 *over elements*, and those with a length equal to  $l_{rope}$  are referred to as *target*  
272 *elements*. The presence of *over elements* can be reduced or eliminated by ap-  
273 propriately choosing the model parameters, including the stiffness coefficient  
274  $k$ , the slack coefficient  $\rho$ , and the time interval  $\Delta t$ . In contrast, the presence  
275 of *loose elements* is determined by the physics of the problem and arises from  
276 ropes that do not experience tension as a result of the applied force field.

277 This paper introduces two methods, Multiple Orders MRA (MO-MRA)  
278 and Repulsive Nodes MRA (RN-MRA), that can be used to reduce the num-  
279 ber of *loose elements* obtained through MRA. These methods can be applied  
280 after MRA to update the final configuration, resulting in a structure with  
281 fewer components of different lengths, making it easier to assemble. When  
282 combined, these methods are referred to as Improved MRA (i-MRA), which,  
283 with a wise selection of model parameters and target lengths, can produce  
284 geometries that are both structurally effective and optimal in terms of ease  
285 of fabrication.

286 *2.1. Multiple Orders MRA*

287 The Multiple Order MRA is a method that aims to reduce the number of  
 288 different structural elements obtained by using classical MRA. The structural  
 289 geometry obtained by applying MRA will be defined by a number of struc-  
 290 tural elements of length  $l_{rope,1}$  and the remaining *loose elements*. The use  
 291 of MO-MRA involves introducing new families of ropes each characterized  
 292 by a length shorter than  $l_{rope,1}$ . The assignment of each rope to each family  
 293 will be determined for each iteration and will be defined as a function of the  
 294 distance between the two nodes connected by the rope. After the geometric  
 295 configuration using the MRA is obtained, consider adding a new family of  
 296 ropes with a final length of  $l_{rope,2} < l_{rope,1}$ . In this scenario, the force  $\vec{F}_{rope}$   
 297 exerted by each rope will depend on the family to which it belongs, and as a  
 298 result, it will be a function of the distance between the two nodes connected  
 299 by the rope. In particular,  $\vec{F}_{rope}$  can be calculated as in the equation 20.

$$\begin{cases} F_{rope} = 0 & \text{if } l < l_{rope,2} \\ F_{rope} = k(l - l_{rope,2}) & \text{if } l_{rope,2} < l \leq \gamma(l_{rope,1} - l_{rope,2}) + l_{rope,2} \\ F_{rope} = 0 & \text{if } \gamma(l_{rope,1} - l_{rope,2}) + l_{rope,2} < l < l_{rope,1} \\ F_{rope} = k(l - l_{rope,1}) & \text{if } l \geq l_{rope,1} \end{cases} \quad (20)$$

300 The resulting equilibrium configuration is iteratively calculated using  
 301 equations (14), (17), and (18) and will correspond to a new structural ge-  
 302 ometry. In the new configuration, the structural element will belong to  
 303 three different element groups, the two characterized by the target lengths  
 304  $l_{rope,1}$  and  $l_{rope,2}$ , and, eventually, the third group composed by the *loose el-*

305 *ements*. The procedure can be repeated adding new families of ropes until  
306 all structural elements correspond to an assigned category. The proposed  
307 method reduces the cost and complexity associated with the construction of  
308 gridshells by grouping structural components with the same length, which  
309 enables the possibility of producing the elements in series and facilitates the  
310 ease and speed of the structure’s construction. On-site management of the  
311 groups of elements is simple and straightforward.

312 The MO-MRA method offers users the flexibility to set parameters such  
313 as the coefficient  $\gamma$  and rope lengths ( $l_{rope,2}$ ,  $l_{rope,3}$ , etc.) to tailor the structural  
314 geometry to their design needs. These parameters are user-defined and allow  
315 for the optimization of the structural design to meet specific construction  
316 or manufacturing constraints. For instance,  $l_{rope,1}$ , defining the first family  
317 of structural elements, can determine the structure’s height (see Figure 3).  
318 However, in cases where cutting steel billets of a constant length is involved,  
319 setting  $l_{rope,1}$  may lead to material wastage. Therefore, the lengths of other  
320 structural element families can be adjusted to minimize waste. Similarly,  
321 the coefficient  $\gamma$  plays a crucial role in assigning the ropes that remain slack,  
322 after the application of the MRA, to different structural element families. It  
323 determines the proportion of ropes with intermediate lengths between the  
324 target lengths of two families that are assigned to each family. The process  
325 of defining the final structural geometry involves configuring both  $\gamma$  and the  
326 target lengths for each family, which can vary widely depending on each  
327 project’s unique requirements. An alternative approach is to create an ob-  
328 jective function based on specific design requirements. This allows for the  
329 formulation of an optimization problem, where the mentioned parameters

330 become design variables. By applying optimization algorithms to solve this  
 331 problem, it is possible to automatically obtain parameter values that best  
 332 align with the design requirements [43].

### 333 2.2. Repulsive Nodes MRA

334 The Repulsive Nodes MRA is a method designed to reduce the number  
 335 of *loose elements* generated by applying the basic MRA. The basic idea is to  
 336 introduce a repulsive force field  $\vec{q}$  between the nodes of the geometric configu-  
 337 ration obtained through the use of MRA. This force field  $\vec{q}$  is introduced after  
 338 the final equilibrium configuration is established using the MRA, which re-  
 339 quires a new iterative computation process to determine the new equilibrium  
 340 condition. The repulsive forces act on the ends of each slack rope, allowing  
 341 the end nodes to move apart as if they possess electrical charges of the same  
 342 sign that repel each other until the rope tensioning. Therefore, for each node  
 343 connected by a slack rope, Equation (7) must be modified by introducing the  
 344 repulsive force field  $\vec{q}$ . As a result, a new system of equations will be obtained  
 345 in which equation (7) will continue to apply for nodes connected to tensioned  
 346 ropes, and equation (21) will be introduced to each node  $i$  connected to slack  
 347 ropes.

$$\vec{R}_i = \vec{p}_i + \vec{q}_i + \sum_{j=1}^{n_i} \left\{ k \cdot \vec{F}_{rope,ji} \right\} - c_i \cdot \vec{v}_i - m_i \cdot \vec{a}_i = 0 \quad (21)$$

348 Equation (21) introduces the repulsive force field  $\vec{q}$  to each node  $i$  con-  
 349 nected to slack ropes. This force field  $\vec{q}$  is linearly proportional to the dif-  
 350 ference between the target length  $l_{rope}$  and the distance between nodes con-  
 351 nected by a slack rope  $l_{ij}$ . To calculate the repulsive force field  $\vec{q}$ , Equation

352 (22) can be used, where  $k_{rep}$  is the proportionality constant that connects  
353 the modulus of the repulsive force to the distance between nodes  $i$  and  $j$ .

$$q_i = -k_{rep}(l_{rope} - l_{ij}) \quad (22)$$

354 The value of the elastic coefficients  $k$  and  $k_{rep}$  depends on many factors.  
355 For example, the coefficient  $k$  must be selected depending on the length of  
356 the ropes, the applied loads, the value of the nodal masses, the time interval  
357  $\Delta t$  defining each iteration, etc. The elastic coefficient  $k$  must be big enough  
358 to avoid the presence of *over elements* and, at the same time, not so big  
359 as to ensure convergence of the system. For the application cases reported  
360 in this paper, a  $k$  value of  $1.2MN/m$  with a  $\Delta t = 0.005s$  was used. These  
361 values can be considered as a starting point for different applications. The  
362 procedure involves to increase the value of  $k$  until no more *over elements* are  
363 present in the final configuration and consequently to reduce  $\Delta t$  in case the  
364 system does not reach the convergence status. Similarly, the value of  $k_{rep}$   
365 must be selected so that repulsive forces between nodes do not produce *over*  
366 *elements* in the final geometric configuration. In the case studies presented  
367 in this work, a  $k_{rep}$  of  $2kN/m$  was used, which can also be used as a first  
368 attempt value for applications other than those presented.

369 It should be noted that the force field introduced in RN-MRA is not a  
370 representation of the actual loads on the structure. Therefore, the resulting  
371 structural shape may differ from the optimal solution obtained through the  
372 pure form-finding process. While the RN-MRA method improves the con-  
373 structability of the structure, it may also result in suboptimal and unattrac-  
374 tive shapes, particularly when applied to models with a significant number of

375 *loose elements*, as shown in Figure 11. Therefore, it is important to apply the  
376 RN-MRA method only to apply minor changes to the geometry obtained by  
377 applying the MO-MRA in order to strike a balance between enhancing con-  
378 structability and achieving the best structural geometry. Ideally, RN-MRA  
379 should be applied to models with few *loose elements* relative to the number  
380 of tensioned ones, and where their length is close to the target length  $l_{rope}$ .

381 In this section, two MRA advances are discussed to produce structural  
382 solutions that are more advantageous in terms of construction convenience.  
383 The i-MRA technique combines these approaches to achieve a geometry with  
384 the optimal balance of structural functionality and ease of construction. The  
385 first approach involves increasing the families of elements in the MO-MRA  
386 until a configuration is obtained in which most of the ropes are under tension.  
387 The second approach, RN-MRA, is then used to improve the geometry by  
388 tensioning the remaining loose elements. As a result, the final shape may  
389 differ slightly from the geometry obtained using MO-MRA alone, but it is  
390 characterized by the smallest possible number of *loose elements*.

391 An example of how the structural geometry evolves gradually from the  
392 shape generated using only MO-MRA initially and then the combination of  
393 MO-MRA and RN-MRA is shown in Figure 20. Here, you can observe how  
394 the two newly introduced methods take effect collaboratively to reduce the  
395 number of structural components with varying lengths.

### 396 **3. Application and results**

397 In this section, four applications of the proposed method on structural  
398 geometries of increasing complexity are presented. A custom Matlab code

399 [44] was developed for applying the proposed methods. The geometries are  
400 represented as quadrilateral meshes where the nodes have a concentrated  
401 mass and the edges are ropes that connect the nodes. The MRA is applied  
402 to each mesh to produce the equilibrium configuration, which represents the  
403 final structural form. By varying the method parameters, different structural  
404 shapes are generated, and the variation of the geometries and the number of  
405 equal elements as a function of the slack coefficient is studied. It is observed  
406 that appropriate parameter selection, especially in the setting of the cor-  
407 rect time interval, allows for the reduction and elimination of *over elements*.  
408 Finally, the structures generated by the various form-finding algorithms dis-  
409 cussed in section 2 are compared in terms of structural analysis as well as the  
410 number of structural components of equal length that constitute the struc-  
411 ture. The comparison shows that the i-MRA allows for reducing the costs  
412 related to the realization of gridshell structures while respecting the struc-  
413 tural optimal solution produced by a pure form-finding method. Overall, the  
414 proposed method is shown to be effective in producing structural solutions  
415 that are both functional and easy to construct.

### 416 3.1. Application 1: Corner constrained square-plan structure

417 The structural geometry of a square gridshell is defined using the MRA  
418 method applied to a square mesh with a side of 15 meters and lines placed  
419 in an orthogonal grid linking nodes at a distance of  $l_{ij} = 1.25m$ , as shown in  
420 Figure 2. The structure is designed to be constrained only in the corners of  
421 the square plan, and the constraints are represented as triangular points in  
422 Figure 2.

423 Although this is a basic case study from a theoretical perspective, the

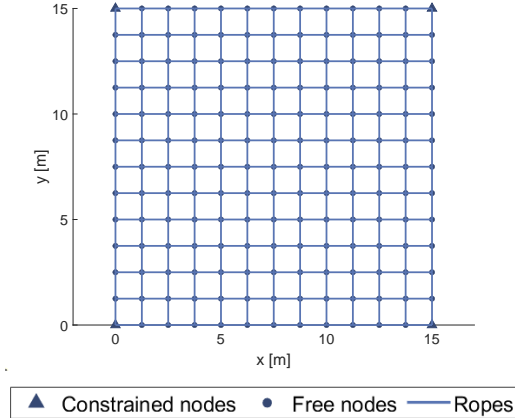


Figure 2: Base mesh for corner constrained square-plan structure

<b>Parameters MRA</b>				
$K[MN/m]$	$m[kg]$	$\zeta[s^{-1}]$	$\Delta t[s]$	$iter_{max}[/math>$
1.2	20	0.95	0.005	100000

Table 1: MRA parameters.

424 structure is demonstration of the ability of this structural typology to gener-  
 425 ate constructively complex shapes from the simplest of forms. The resulting  
 426 structure is composed of 312 structural elements and 169 nodes. By using an  
 427 appropriate parameter setting, as detailed in Table 1, it is possible to obtain  
 428 a structural geometry where all beam elements have the same length, with a  
 429 tolerance of one centimeter.

430 The ratio of the maximum horizontal structural dimension to the height  
 431 of the structure is referred to as the degree of sag, denoted as  $\eta$ . By varying  
 432 the slack coefficient  $\rho$ , it is possible to generate different structural shapes  
 433 with varying degrees of sag. The relationship between the degree of sag  $\eta$   
 434 and the slack coefficient  $\rho$  for the specific geometric configuration examined

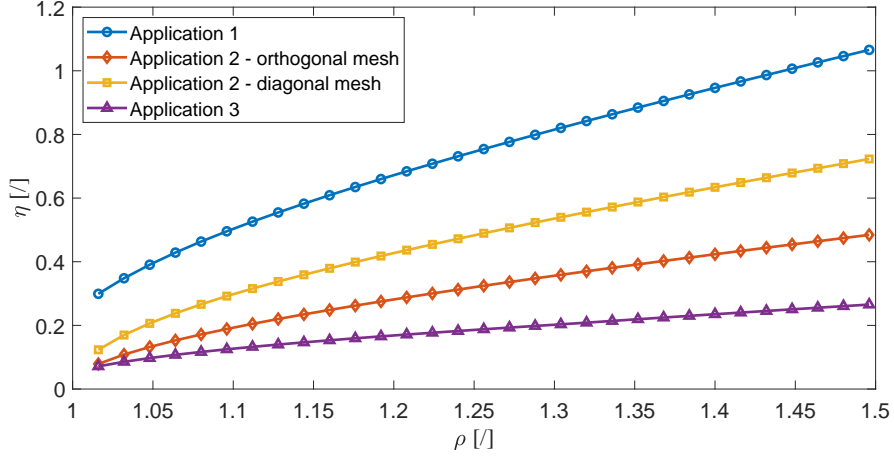
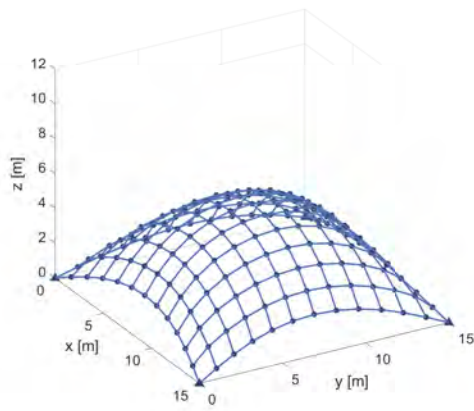


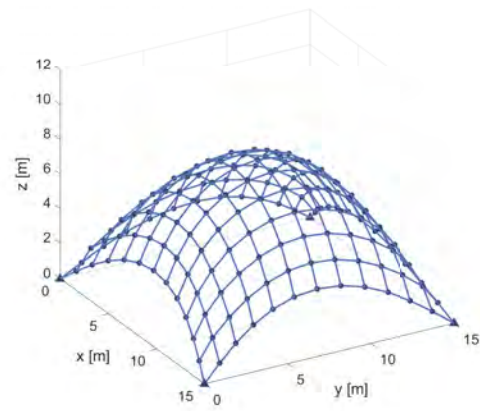
Figure 3: Degree of sag  $\eta$  as function of the slack coefficient  $\rho$

435 in this section is illustrated in Figure 3. The graph clearly indicates that for  
 436 values of  $\rho > 1.1$ , the height of the structure increases in proportion to the  
 437 slack coefficient. The graph can be utilized by designers to determine the  
 438 target length  $l_{rope}$  as a function of the design structural height.

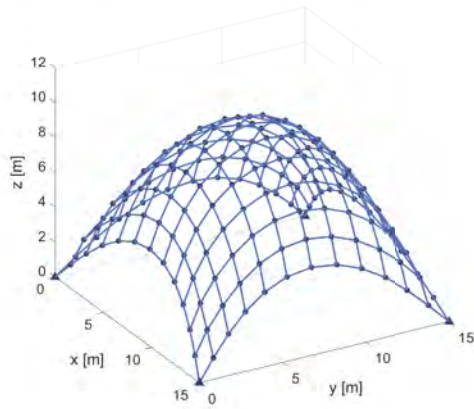
439 Figure 4 displays four different geometric configurations that can be gen-  
 440 erated from the same basic mesh, each having a distinct slack coefficient  $\rho$   
 441 and consequently a different height. It is noteworthy that having the ability  
 442 to produce several geometries from a single basic plan is crucial. The choice of  
 443 a specific geometric form over another may be influenced by various factors,  
 444 such as architectural or structural considerations. The parameters utilized to  
 445 create the different structural geometries are listed in Table 1. It is evident  
 446 that each geometric configuration necessitates a specific number of iterations  
 447 *iter*, and the more the final configuration varies from the initial one, the more  
 448 iterations are needed. Therefore, higher structures require more iterations  
 449 and, as a result, longer computation times.



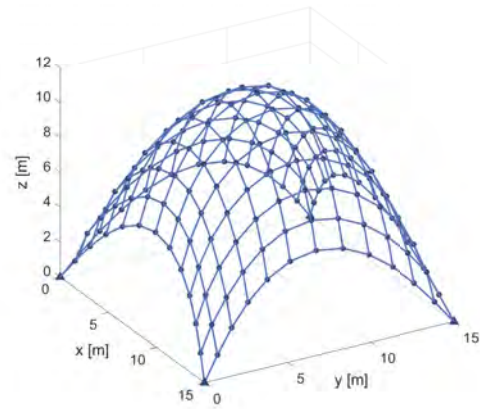
(a)  $\rho = 1.06$



(b)  $\rho = 1.12$



(c)  $\rho = 1.20$



(d)  $\rho = 1.28$



Figure 4: MRA application on corner constrained square-plan structure for different slack coefficients  $\rho$ .

450 *3.2. Application 2: Boundary constrained square-plan structure*

451 In the second scenario, a square mesh with a side length of 15 meters  
452 was used, which is similar to the one shown in Section 3.1. However, in  
453 this case study, all points on the mesh’s edge were constrained, unlike the  
454 previous scenario. This means that there are fewer options to adapt the final  
455 design due to the increased restrictions placed on the structure. Despite this,  
456 the MRA method alone still enabled designs with a significant proportion of  
457 structural components having the same length. The method’s robustness  
458 was demonstrated by creating two different starting configurations from the  
459 same edge constraints. The first configuration used a square grid mesh with  
460 perpendicular elements connecting nodes at a distance of  $1.25m$ , as shown  
461 in Figure 5a. In the second case, the mesh was constructed by connecting  
462 the constrained nodes on the edges with diagonal elements, resulting in a  
463 final mesh with more nodes and structural components, as shown in Figure  
464 5b. The two meshes differ significantly in terms of node and component  
465 quantity and layout. The first case has 165 nodes and 264 elements arranged  
466 parallel to the base square’s sides, while the second case has 313 nodes and  
467 576 elements aligned at a  $45^\circ$  angle.

468 The figures presented in Figure 7 illustrate four examples of structural  
469 geometries that were derived from the same basic mesh in Figure 5a. By  
470 varying the slack coefficient  $\rho$ , it is apparent that even minor increases in  
471 structural complexity, which are solely determined by the arrangement of  
472 constraints, make it impossible to achieve 100 percent equal-length structural  
473 elements using the basic MRA. The structural components with lengths that  
474 differ from the target length  $L_{rope}$  are highlighted in red in Figure 7.

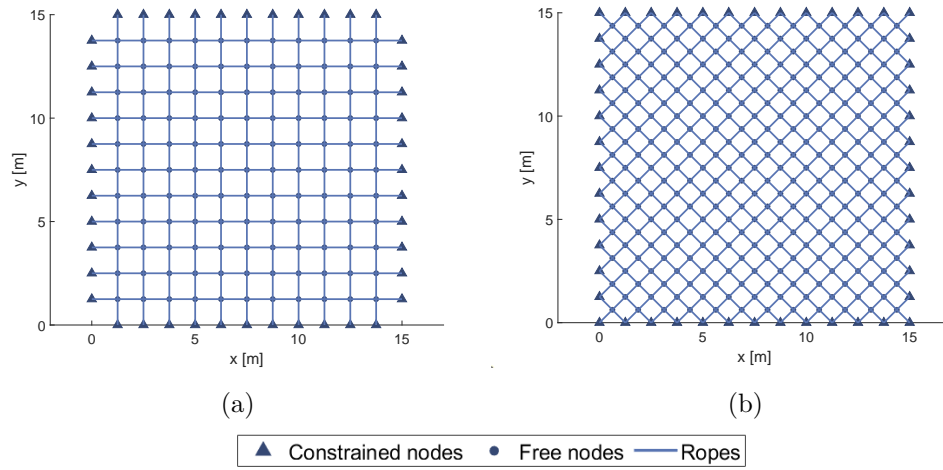


Figure 5: Base mesh for boundary-constrained square-plan structure

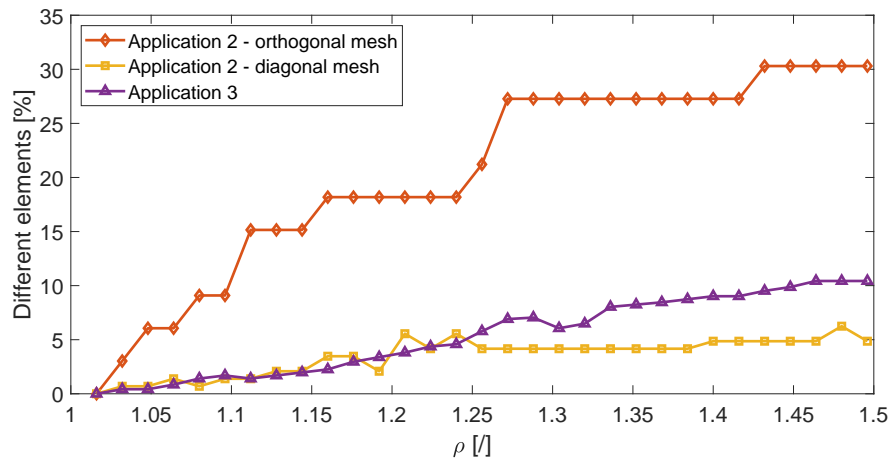


Figure 6: Percentage of loose ropes as a function of the slack coefficient  $\rho$

<b>Parameters RN-MRA</b>		
$K[kN/m]$	$\Delta t[s]$	$iter_{max}[/math>$
2.0	0.005	3000

Table 2: RN-MRA parameters

475 The graph in Figure 6 illustrates how the number of different elements  
476 increases proportionally to the slack coefficient  $\rho$ . When  $\rho = 1.5$ , 30% of  
477 elements have lengths different from the target one. However, due to the  
478 simple and symmetrical nature of the initial geometry, managing the presence  
479 of these elements during construction should be straightforward. Despite the  
480 simple geometry, the provided example demonstrates that *loose ropes* can be  
481 generated using the basic MRA. For instance, in Figure 7c, which has  $\rho =$   
482 1.20, the structure comprises 6 different structural elements, even considering  
483 the structural symmetry. Nearly 20% of elements have a length  $l \neq 1.50m$ .  
484 In such cases, the usage of i-MRA can help reduce the number of different  
485 structural components. Figure 9 shows the application of i-MRA to calculate  
486 the structure in Figure 7c. The use of i-MRA with the slack coefficients  
487  $\rho = (\rho_1; \rho_2; \rho_3)$  results in a structure comprising only three different structural  
488 element types. Table 2 reports the parameters used to apply the repulsive  
489 nodes MRA (RN-MRA).

490 In the geometry depicted in Figure 9a, where the slack coefficients are  
491 set to  $\rho = (1.20; 1.12; 1.06)$ , every element has a length of either 1.5, 1.4,  
492 or 1.3 meters, demonstrating the clear advantages of using i-MRA. Even  
493 in this relatively simple scenario, the method allows for a reduction in the  
494 number of element types from 6 to just 3, resulting in 50% reduction in the

495 number of element types that need to be managed during construction, even  
496 when considering a precision of just one centimeter. Figure 9b presents the  
497 results of applying i-MRA to the same structural scenario but with different  
498 slack coefficients set at  $\rho = (1.20; 1.08; 1.00)$ . This configuration generated  
499 a structure composed exclusively of elements measuring 1.50, 1.35, or 1.25  
500 meters in length, and once again, only three different structural element types  
501 were required. This further highlights the versatility of i-MRA in allowing  
502 designers to customize the parameters to achieve various configurations that  
503 meet project requirements without increasing the complexity of construction.

504 Histograms were employed to illustrate the distribution of element lengths,  
505 aiming to enhance understanding of the variation in the quantity of different  
506 types of structural elements. Specifically, Figure 8 presents the distributions  
507 of element lengths for the case studies depicted in Figure 7. The histograms  
508 clearly demonstrate how both the types of structural elements and their  
509 lengths increase with the rise in the slack coefficient. Additionally, Figure  
510 10 illustrates the distribution of element lengths corresponding to the cases  
511 depicted in Figure 9. In this case, it is evident that the use of the i-MRA  
512 results in a significant reduction element typologies.

513 An example of misapplication of the method is shown in Figure 11. In this  
514 case, the RN-MRA method was applied directly after MRA, without utilising  
515 MO-MRA as an intermediate step. The geometry obtained through MRA  
516 had excessive *loose elements*, making it unsuitable for direct application of  
517 RN-MRA. The result is a geometry that does not find a good balance of  
518 convenience in construction and structural efficiency.

519 Figure 12 displays four examples of basic MRA applied to the base mesh



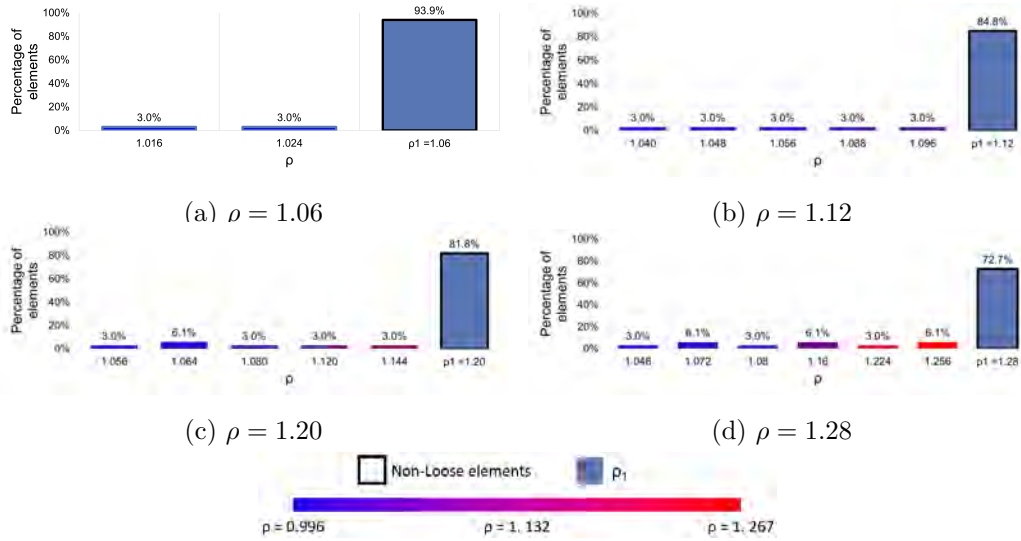


Figure 8: Application 2 with orthogonal base mesh: Structural element lengths distribution applying the MRA.

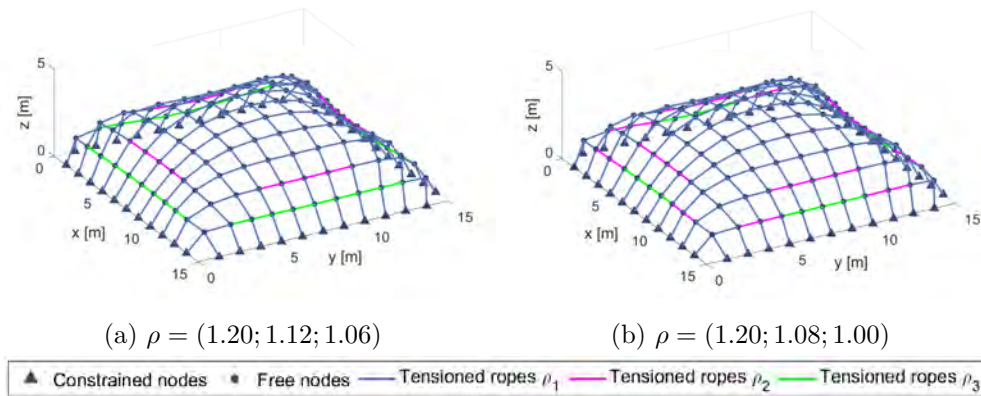


Figure 9: i-MRA application on boundary constrained square-plan structure with orthogonal mesh for different slack coefficients  $\rho$ .

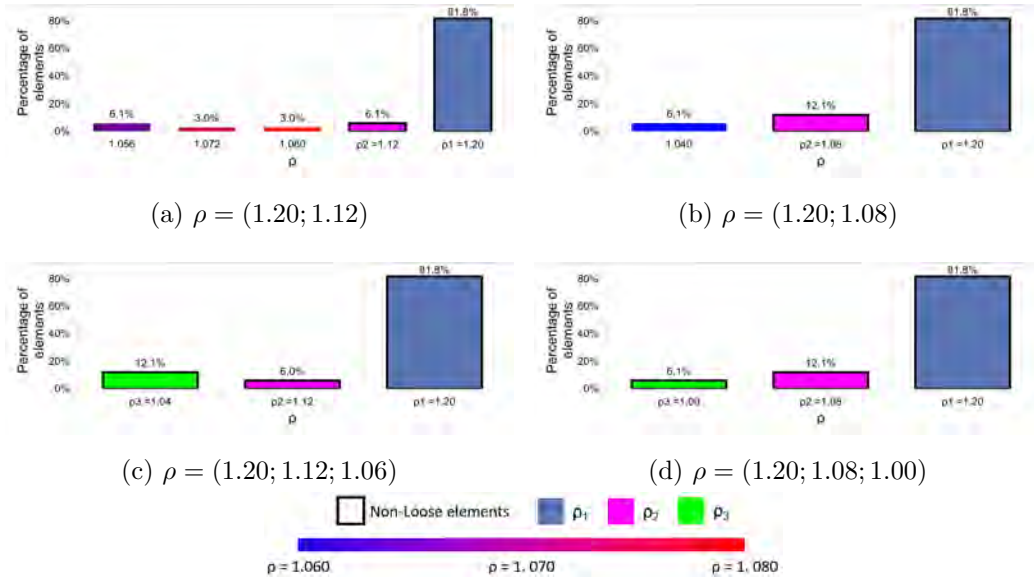


Figure 10: Application 2 with orthogonal base mesh: Structural element lengths distribution applying the i-MRA.

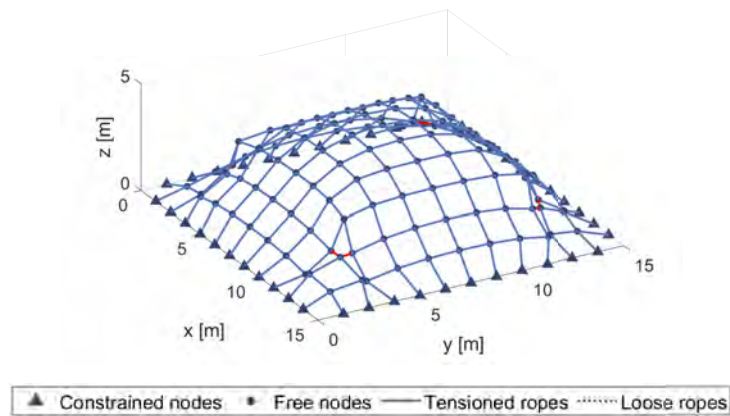


Figure 11: Incorrect application of RN-MRA application on boundary constrained square plan structure with orthogonal mesh and  $\rho = 1.20$ .

520 from Figure 5*b*, generated by varying the slack coefficient. It is clear from this  
521 scenario that the resulting structures differ greatly from those in the previous  
522 case, both in terms of shape regularity and degree of sag  $\eta$ . The degree of sag  
523  $\eta$  is plotted as a function of the slack coefficient  $\rho$  in the graph in Figure 3.  
524 The function trend is identical to that obtained with other basic geometries,  
525 but the obtained values here are quantitatively different. Diagonal gridshells  
526 are typically higher than those produced by the orthogonal mesh with the  
527 same slack coefficient. Additionally, Figure 6 reports the percentages of el-  
528 ements that differ from the target ones after applying basic MRA. In this  
529 scenario, the number of different elements out of the total is evidently smaller  
530 than in the previous case, with a maximum of 5% compared to the previous  
531 maximum of 30%. Moreover, for specific slack coefficient values, privileged  
532 configurations are revealed. The function representing the percentage of dif-  
533 ferent elements as a function of the slack coefficient presents local minima  
534 for certain values of  $\rho$ , which may be advantageous from a design perspective  
535 as they enable the reduction of the number of different structural element  
536 classes. Comparing the cases presented in this section, it is evident that the  
537 choice of mesh and initial parameters is critical to the final design output.  
538 A good initial choice of parameters can have a great influence on the final  
539 structural geometry, regardless of the form-finding method used to calculate  
540 it. In Figure 13, the distribution of element lengths is illustrated for the  
541 case studies with different slack coefficients depicted in Figure 12. This fig-  
542 ure highlights once again that increasing the slack coefficient  $\rho$  results in an  
543 increase in the number of element typologies.

544 The application of i-MRA to the geometry with  $\rho = 1.20$  provided in Fig-

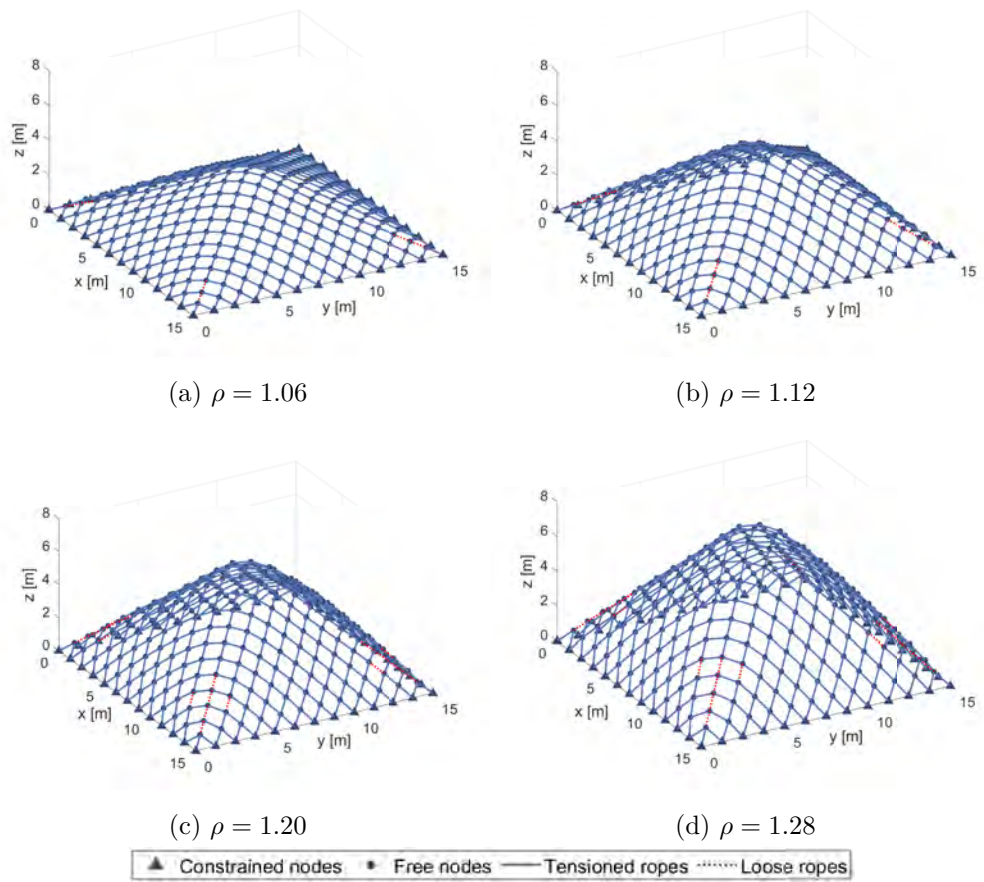


Figure 12: MRA application on boundary constrained square-plan structure with diagonal mesh, for different slack coefficients  $\rho$ .

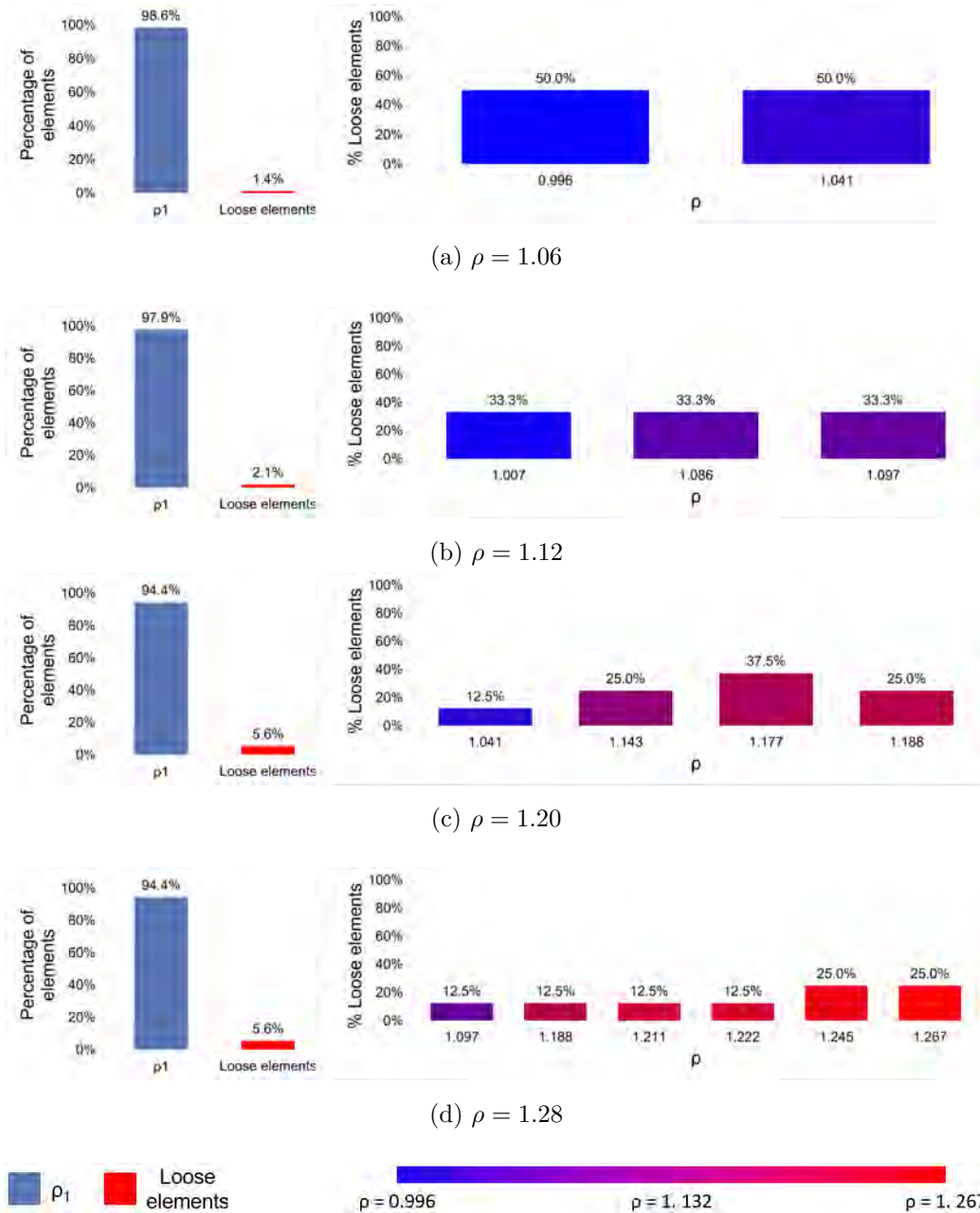


Figure 13: Application 2 with diagonal base mesh: Structural element lengths distribution applying the MRA.

545 ure 12c is presented in Figure 14. The geometry produced by the basic MRA  
546 results in 5 different types of structural elements assuming structural symme-  
547 try is taken into account. However, the i-MRA approach allows for reducing  
548 the variety of structural elements even in this straightforward situation. The  
549 gridshell calculated with the i-MRA and slack coefficient  $\rho = (1.2; 1.09)$  can  
550 be realized using only 2 types of structural elements, demonstrating the effec-  
551 tiveness of the newly presented method in reducing the variety of elements to  
552 be handled during the construction process. Additionally, in Figure 14a, it is  
553 highlighted that using only MO-MRA allows for obtaining a geometry com-  
554 posed of 3 types of elements. The power of i-MRA can be further appreciated  
555 by obtaining a structure composed of only two types of elements through the  
556 wise use of RN-MRA properly combined with MO-MRA, as shown in Fig-  
557 ure 14b. The reduction in the number of element typologies resulting from  
558 the application of i-MRA is evident in Figure 23, where the distribution of  
559 element lengths is represented by the mean of histogram graphs.

560 Figures 16 and 17 present a comparison of the structural analysis results  
561 obtained with basic MRA and i-MRA methods for S275 structural steel grid-  
562 shells composed of *CHS 200 5* profiles and loaded on each node with a unity  
563 load in the gravitational direction. These figures show, on the left, the anal-  
564 yses conducted on structures obtained with basic MRA and, on the right,  
565 those obtained with i-MRA. Specifically, Figure 16 shows the analyses for the  
566 configuration shown in Figure 7c on the left, and those for the configuration  
567 in Figure 9a on the right. Figure 17 shows the analyses of the structure in  
568 Figure 12c on the left, and the analyses of the structure in Figure 14b on  
569 the right. The comparisons in both figures are presented in terms of axial

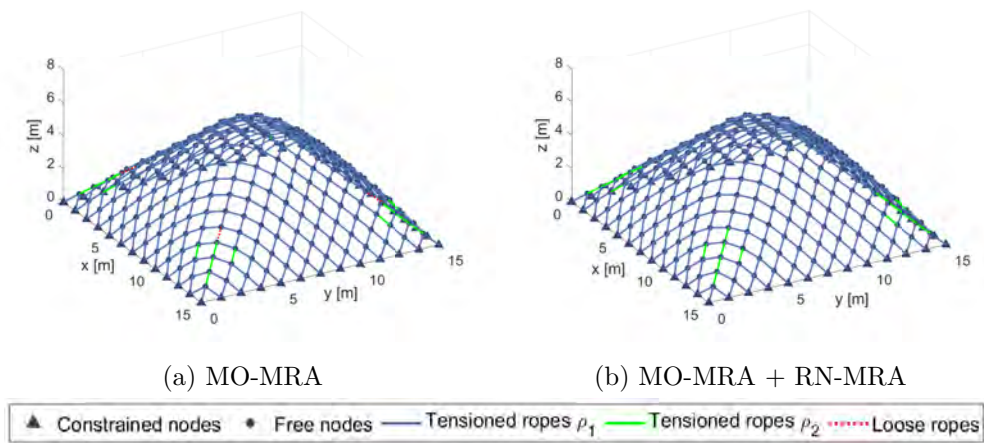


Figure 14: i-MRA application on boundary constrained square-plan structure with diagonal mesh.

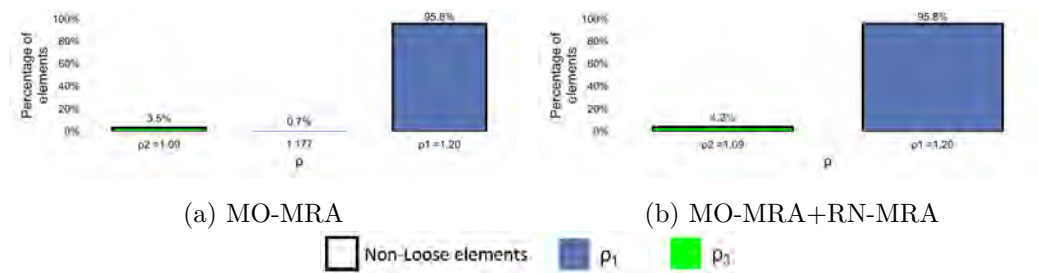


Figure 15: Application 2 with diagonal base mesh: Structural element lengths distribution applying the i-MRA.

570 force at the top, bending moment in the middle, and Von Mises stress at the  
571 bottom.

572 The i-MRA produces geometries that deviate from the funicular struc-  
573 tural form. However, the differences in terms of stresses between the i-MRA  
574 and basic MRA geometries appear to be minimal. Although the geometries  
575 are different, they have similar structural behavior. In the cases presented  
576 in this section, the i-MRA produces a significant improvement in terms of  
577 minimizing the types of elements that make up the structure. The cost of  
578 the geometric variation produced from the viewpoint of structural optimum  
579 seems to be small, as demonstrated by the reported comparisons.

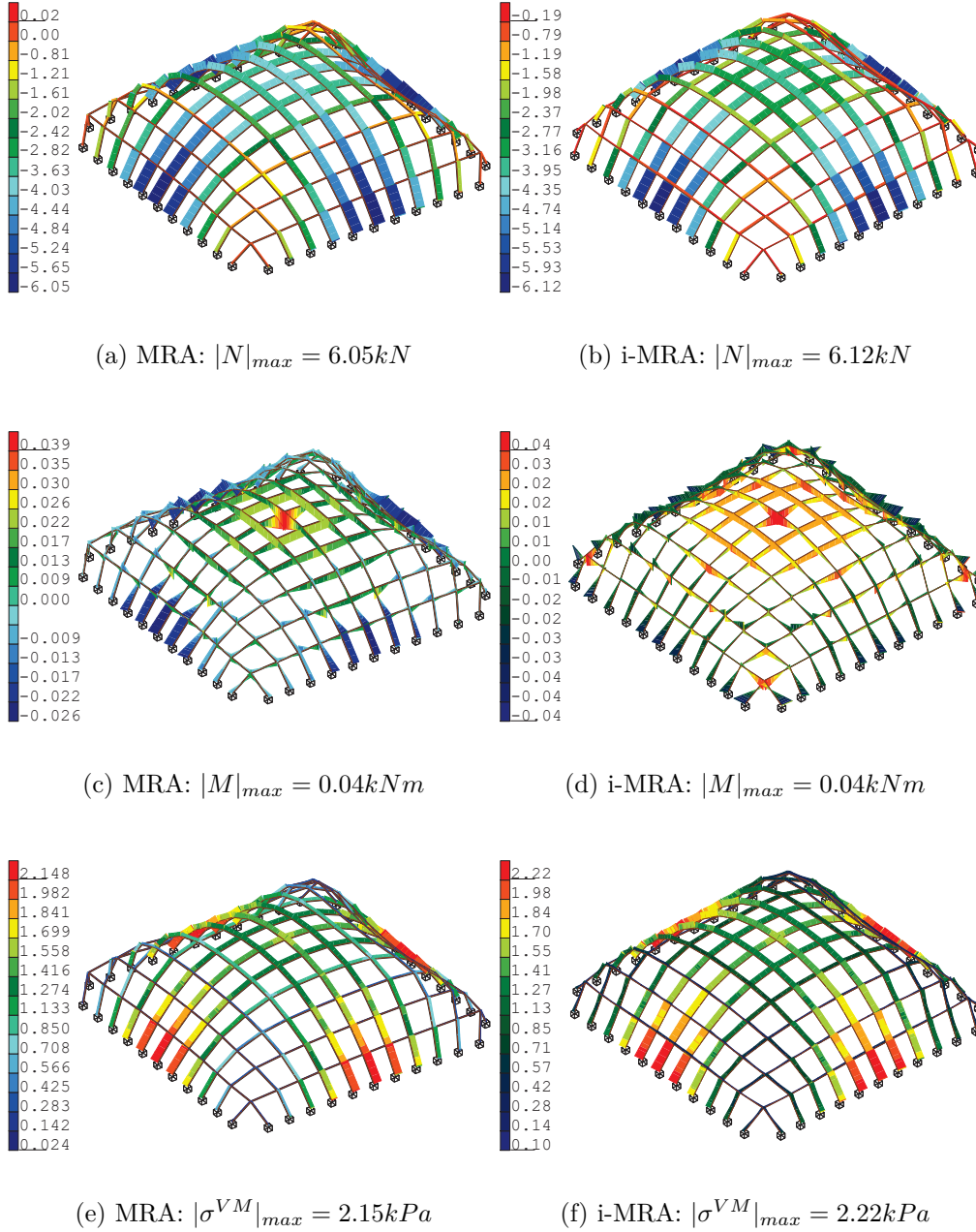


Figure 16: Structural analysis performed on the structures obtained by applying basic MRA (left) and i-MRA (right) on the application example with orthogonal mesh in Section 3.2. Comparison in terms of axial force [kN] (top), bending moment [kNm] (middle) and Von Mises stress [kPa] (bottom).

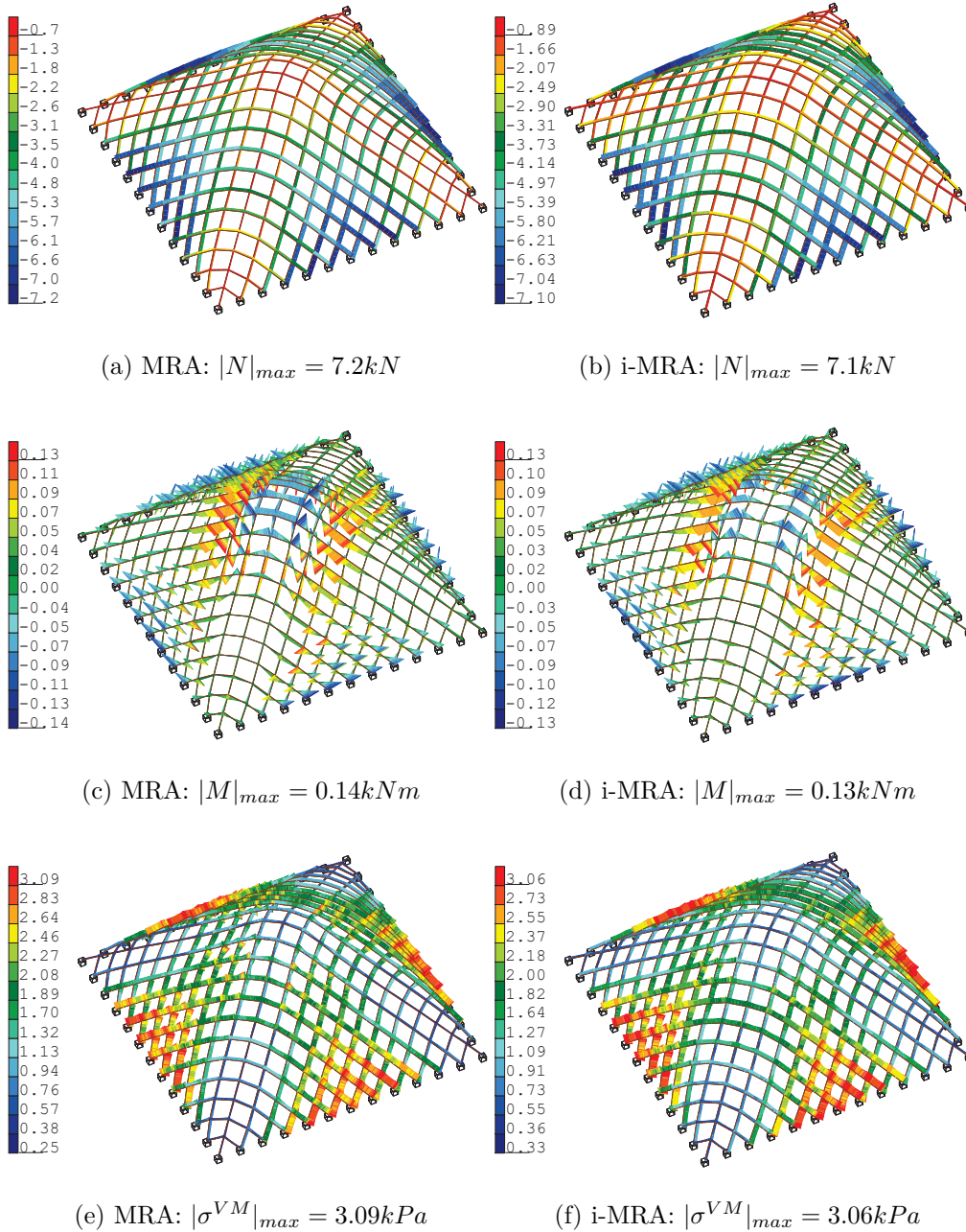


Figure 17: Structural analysis performed on the structures obtained by applying basic MRA (left) and i-MRA (right) on the application example with diagonal mesh in Section 3.2. Comparison in terms of axial force [kN] (top), bending moment [kNm] (middle) and Von Mises stress [kPa] (bottom).

580 *3.3. Application 3: Symmetrical structure with a non-canonical geometric*  
581 *plan and opening in the center.*

582 The third example structure features a ground plan that is divided into  
583 five primary zones. The main zone is a large rectangular space with a square  
584 opening in the center, while four smaller rectangular areas overlap the main  
585 one at the corners of the central zone. Figure 18 displays the structure’s mesh,  
586 which consists of 1419 elements measuring 1.20 meters in length connecting  
587 the 760 nodes. The structure is constrained on each outer corner as well as  
588 around the entire perimeter of the central hole. This scenario was chosen to  
589 introduce some complexity and demonstrate how the approach can handle  
590 complex situations. Nevertheless, this structural design has a regular plan  
591 characterized by two axes of symmetry. Similar to the previous cases, the  
592 relationship between the slack coefficient and the height of the structure,  
593 as determined by the form-finding process, was investigated. As depicted  
594 in Figure 3, the height trend as a function of the slack coefficient exhibits  
595 qualitatively the same behavior as that observed in the simpler examples,  
596 even for a complex structural geometry like the one under consideration.

597 Figures 19 and 20a show four examples of structural geometries obtained  
598 with different slack coefficients. It can be observed that the number of *loose*  
599 *ropes*, which corresponds to the number of structural elements of varying  
600 lengths, increases as the slack coefficient increases. Figure 6 depicts this  
601 trend, revealing that the progression is not monotonically increasing and  
602 that there are preferred configurations with a smaller percentage of different  
603 elements.

604 This section effectively demonstrates the potential of i-MRA through

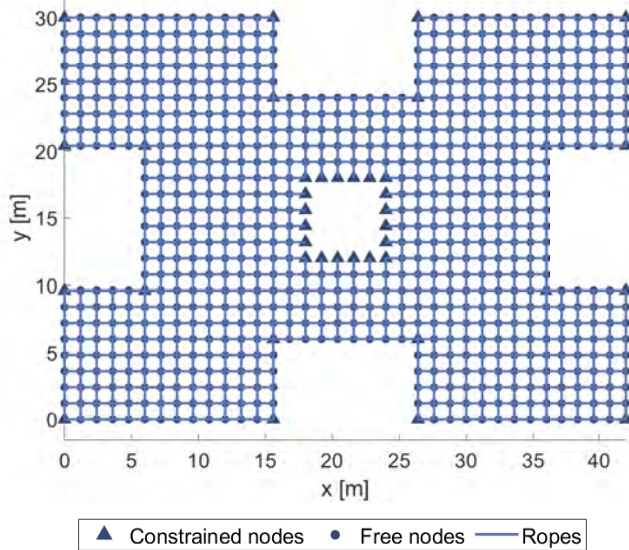
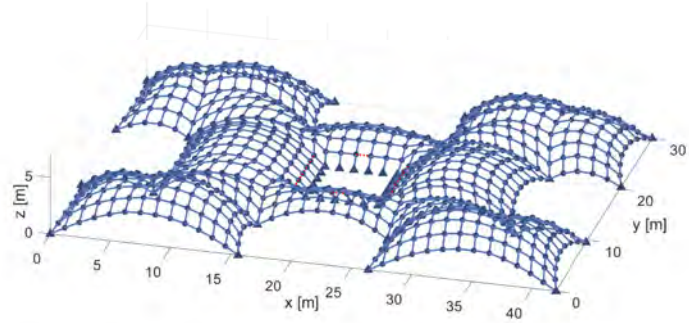
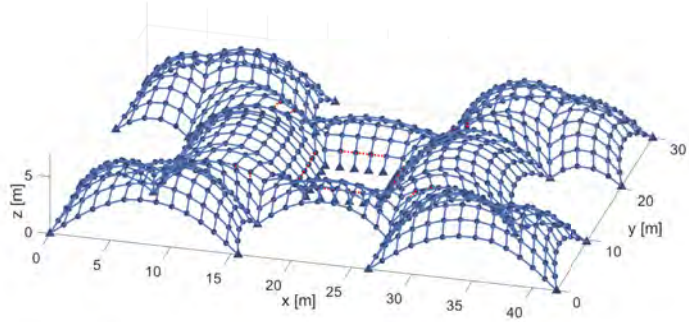


Figure 18: Base mesh symmetrical structure with non-canonical geometric plan and opening in the center.

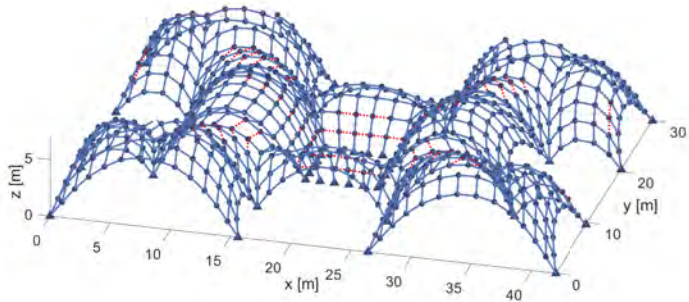
605 the analysis of the geometry obtained with a slack coefficient of  $\rho = 1.20$ , as  
 606 shown in Figure 20a. The analysis reveals that over 3.5% of the structural el-  
 607 ements are shorter than the target length. However, since the entire structure  
 608 can be completed using only 11 different types of components, the basic MRA  
 609 is deemed highly efficient. By incorporating structural symmetries and regu-  
 610 lar initial meshes, the number of required element types can be significantly  
 611 reduced. Figure 20 illustrates the structural configurations obtained in the  
 612 successive steps of the i-MRA application. In particular, Figure 20a depicts  
 613 the application of MO-MRA with two orders of structural elements. This  
 614 configuration is obtained by setting target lengths  $L_{rope} = (1.44m; 1.35m)$ ,  
 615 corresponding to slack coefficients  $\rho = (1.20; 1.13)$ . This initial step re-  
 616 duces the required types of elements from 11 to 10. Figure 20b shows



(a)  $\rho = 1.06$



(b)  $\rho = 1.12$



(c)  $\rho = 1.28$

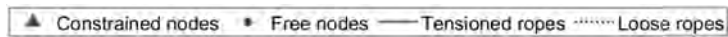
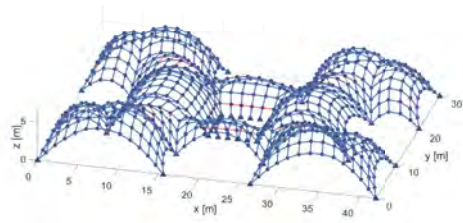


Figure 19: MRA application on symmetrical structure with a non-canonical geometric plan and opening in the center, for different slack coefficients: (a)  $\rho = 1.06$ , (b)  $\rho = 1.12$ , (c)  $\rho = 1.28$ .

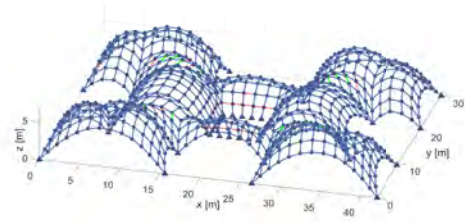
617 the next step, which utilizes MO-MRA with three distinct target lengths,  
618  $L_{rope} = (1.44m; 1.35m; 1.30m)$ , corresponding to  $\rho = (1.20; 1.13; 1.08)$ . As a  
619 result, a geometry is produced that can be constructed using only 5 different  
620 types of pieces, further reducing the required element typologies from 10 to  
621 5. Finally, the RN-MRA is applied to the system in Figure 20b, taking into  
622 consideration that the loose ropes are only slightly shorter than the target  
623 lengths. This results in the geometry depicted in Figure 20c, which can be  
624 constructed using only 3 types of structural elements.

625 The changes in the distribution of element lengths for the distinct case  
626 studies in Figures 19 and 20 are depicted in Figures 21, 22, and 23. In  
627 particular, in Figure 21, the histograms illustrate the distribution of lengths  
628 after the application of the basic MRA. In addition, the reduction in element  
629 typologies resulting from the application of MO-MRA is evident in the distri-  
630 butions depicted in Figure 22. Finally, in Figure 21, the lengths distribution  
631 for the final configuration obtained through the complete i-MRA application  
632 is presented.

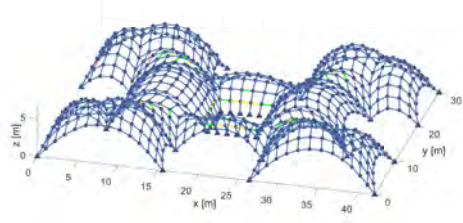
633 The third example highlights the significant benefits of using i-MRA on  
634 complex-shaped structures by simplifying the construction process manage-  
635 ment. By adopting this approach, the number of structural element classes  
636 that need to be managed on the construction site can be reduced from a  
637 maximum of 11 different types of components to just 3. Minor adjustments  
638 are made to the structural shape obtained with the basic MRA to achieve  
639 this reduction. The final geometry of the structure exhibits regularity and  
640 consistency with shapes determined using only form-finding techniques. This  
641 is crucial as it allows the structure to avoid significant deviations from the



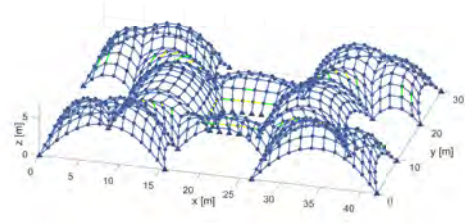
(a) MRA  $\rho = 1.20$



(b) MO-MRA  $\rho = (1.20; 1.13)$



(c) MO-MRA  $\rho = (1.20; 1.13; 1.08)$



(d) Complete i-MRA  $\rho = (1.20; 1.13; 1.08)$

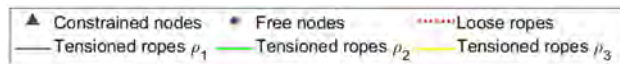
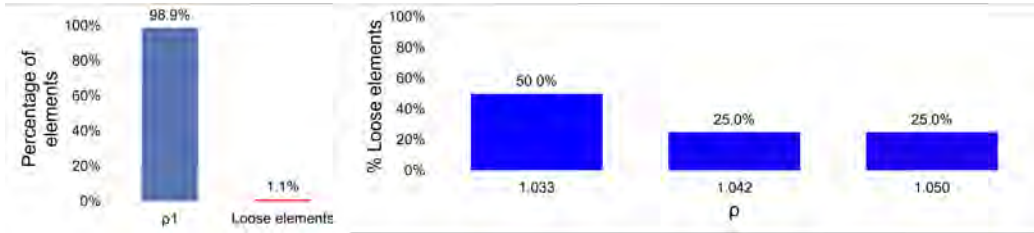
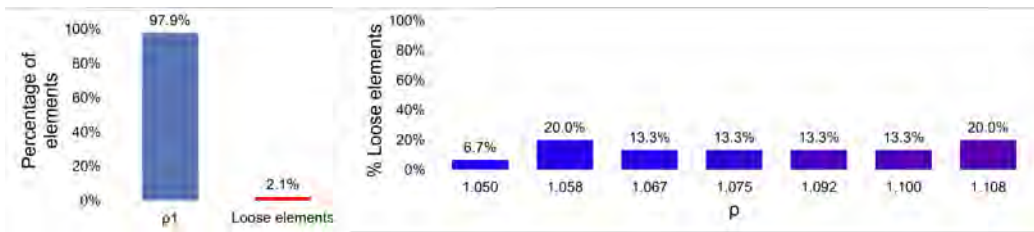


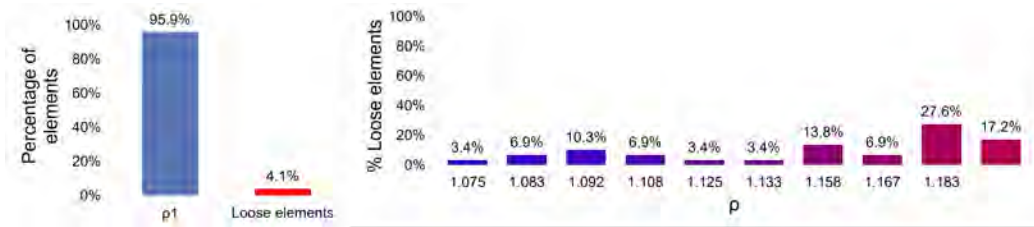
Figure 20: i-MRA application on symmetrical structure with a non-canonical geometric plan and opening in the center.



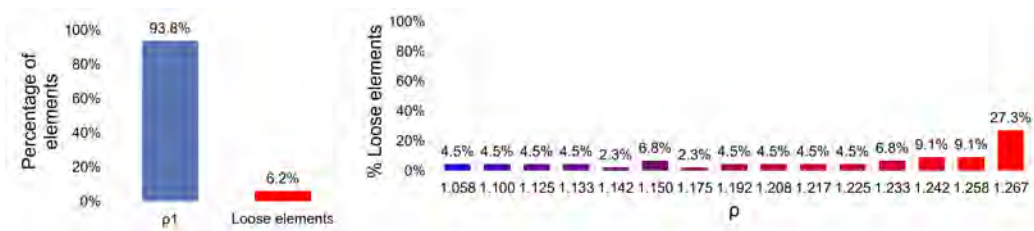
(a)  $\rho = 1.06$



(b)  $\rho = 1.12$



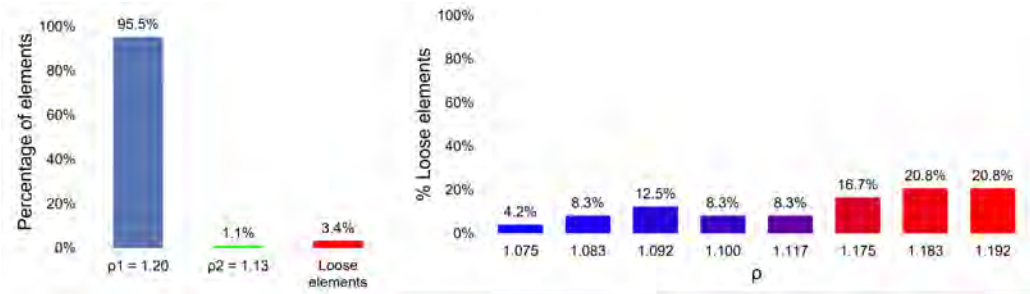
(c)  $\rho = 1.20$



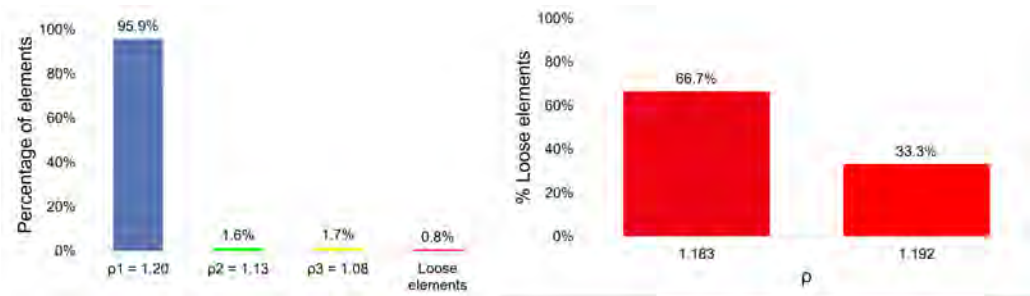
(d)  $\rho = 1.28$



Figure 21: Application 3: Structural element lengths distribution applying the MRA.



(a) MO-MRA  $\rho = (1.20; 1.13)$



(b) MO-MRA  $\rho = (1.20; 1.13; 1.08)$



Figure 22: Application 3: Structural element lengths distribution applying the MO-MRA.

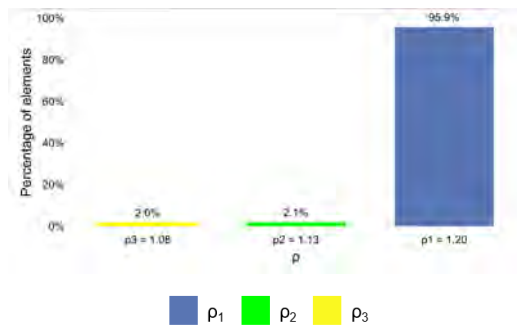
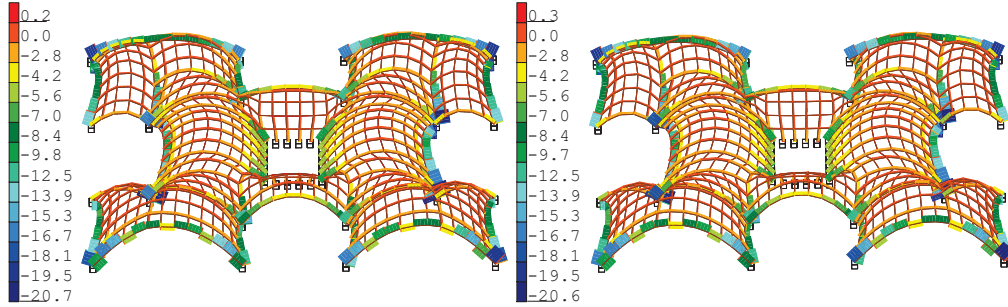


Figure 23: Application 3: Structural element lengths distribution applying the complete i-MRA.

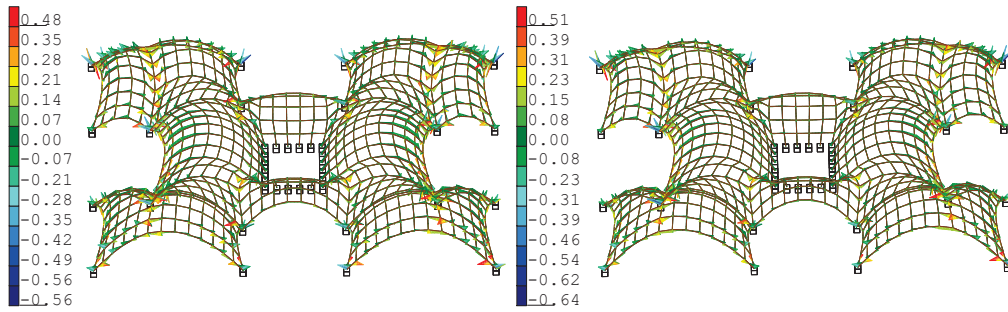
642 funicular shape, which represents the optimal shape from a structural point  
643 of view.

644 The structural analyses presented in Figure 24 demonstrate that the ge-  
645 ometries produced by basic MRA (on the left) and i-MRA (on the right) are  
646 very similar in terms of axial force (top), bending moment (middle), and Von  
647 Mises stress (bottom). This indicates that the deviations from the funicular  
648 shape obtained with i-MRA are minimal. In this case, the use of i-MRA  
649 results in a reduction of the structural components by five times, while the  
650 static behavior of the structure remains virtually unchanged.



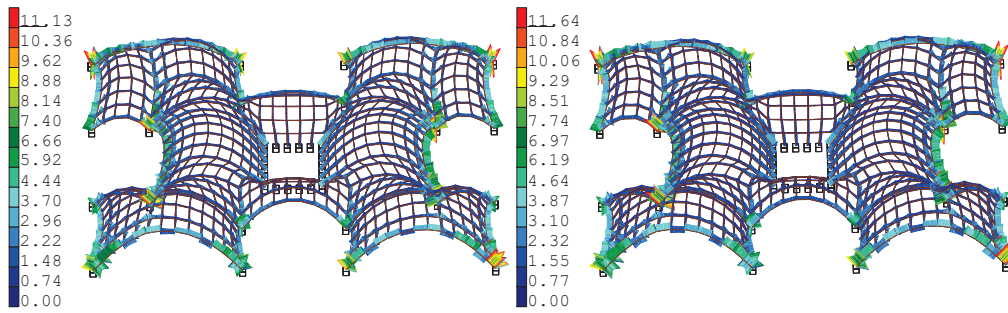
(a) MRA:  $|N|_{max} = 20.7kN$

(b) i-MRA:  $|N|_{max} = 20.6kN$



(c) MRA:  $|M|_{max} = 0.56kNm$

(d) i-MRA:  $|M|_{max} = 0.64kNm$



(e) MRA:  $|\sigma^{VM}|_{max} = 11.13kPa$

(f) i-MRA:  $|\sigma^{VM}|_{max} = 11.64kPa$

Figure 24: Structural analysis performed on the structures obtained by applying basic MRA (left) and i-MRA (right) on the application example in Section 3.3. Comparison in terms of axial force [kN] (top), bending moment [kNm] (middle) and Von Mises stress [kPa] (bottom).

651 *3.4. Application 4: Free-form geometry*

652 The final application example aims to evaluate the effectiveness of the  
653 proposed approach in a highly general scenario. The method is applied by  
654 considering a base plan that is defined by a free-form curve, and the mesh  
655 is generated automatically using parametric design software. The analysis  
656 focuses on two types of meshes: the quadrangular mesh and the mesh formed  
657 by hexagonal and pentagonal elements. The meshes are generated with the  
658 goal of covering the reference surface as smoothly as possible. In this partic-  
659 ular example, the basic mesh's constituent parts result in various sizes and  
660 shapes due to the surface's irregular layout. Consequently, this is the most  
661 complex application of MRA, as the proposed objective is to obtain equal  
662 structural elements from a geometry composed of different elements.

663 Both meshes presented in this section are made up of edges with an  
664 average length of about 1.50m. However, the elements that make up the  
665 quadrangular mesh in Figure 25a range in length from a minimum of about  
666 0.80m to a maximum of about 2.30m, resulting in a considerable degree of  
667 variability in the starting elements.

668 In this example, each rope has its unique slack coefficient since the defi-  
669 nition of the slack coefficient  $\rho$  is based on the initial distance between nodes  
670 (Equation 23) and takes into account that this distance varies for each pair  
671 of connected nodes. This implies that the coefficient is depicted as a vector  
672 with a length equal to the total number of ropes. To offer a comprehensive  
673 measure,  $\rho_{avg}$  is defined as the average of all the slack coefficients within  
674 the vector. Therefore, the definition of  $\rho_{avg}$  is reported in the following  
675 expression:

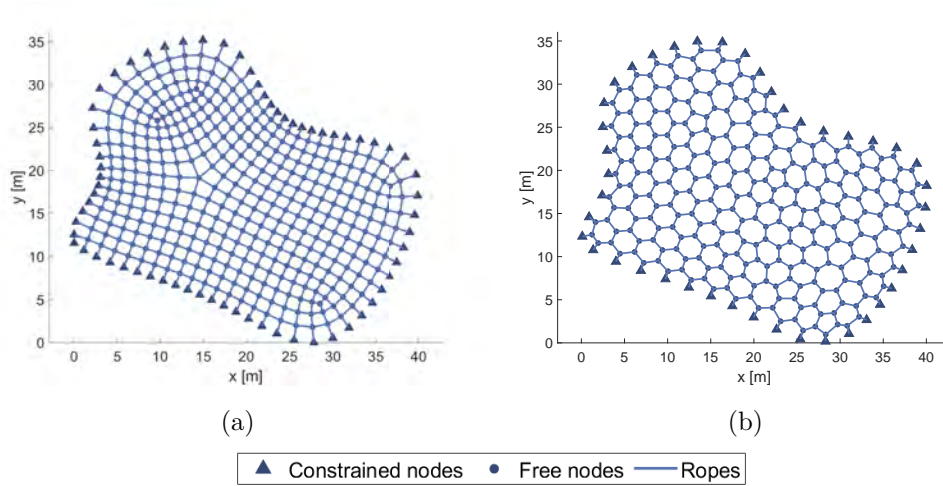


Figure 25: Different base mesh for free-form structure

$$\rho_{avg} = \frac{\sum_{i=1}^{n_{ropes}} (\rho_i)}{n_{ropes}} \quad (23)$$

676 The structural configuration obtained using the basic MRA with a  $\rho_{avg} =$   
677 1.20 for the quadrangular mesh case (Figure 25a) is shown in Figures 26a  
678 and 26c. In this case, red is used to indicate structural elements whose final  
679 length deviates from the target length of  $L_{rope} = 1.78m$  (*loose ropes*). These  
680 elements constitute more than 13% of the 750 structural components that  
681 form the gridshell due to the basic geometry irregularities. As a result, more  
682 than 100 different structural elements are different from the target one in  
683 the actual structure. Although this may be manageable on the construction  
684 site, it can be challenging for generic and complex structural forms, mak-  
685 ing construction phase management more difficult than observed in previous  
686 examples.

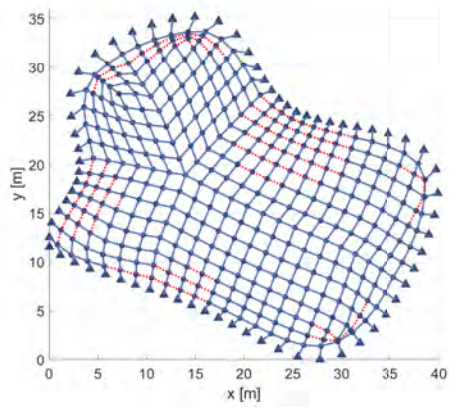
687 The distribution of lengths for the structural elements in this case study is

688 depicted in Figure 27. The structure is characterized by 44 different element  
689 typologies, highlighting the variability of element types in this specific case  
690 study.

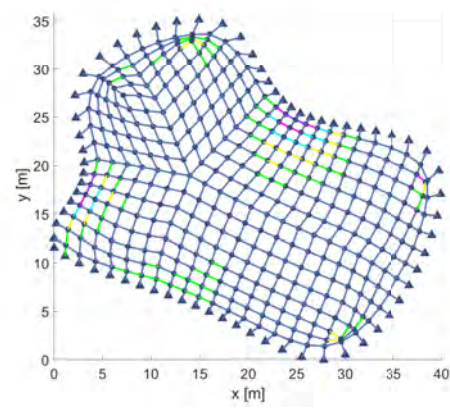
691 However, the structural configuration obtained by applying the i-MRA  
692 presented in this paper is shown in Figures 26*b* and 26*d*. The improvement  
693 achieved in this scenario is significant. The technique allowed for the calcula-  
694 tion of a structural geometry that can be realized by employing only 6 struc-  
695 tural component types of length  $L_{rope} = [1.78; 1.58; 1.45; 1.35; 1.25; 1.15]m$ .  
696 Figure 28 represents the distribution of structural elements among the 6 tar-  
697 get lengths. This result is impressive and demonstrates how the techniques  
698 presented in Section 2 can substantially reduce construction complexity.

699 The results of the structural analyses presented in Figure 4 indicate that  
700 the changes in structural geometry achieved through i-MRA do not cause a  
701 significant increase in stresses. The structure calculated with i-MRA (right)  
702 experiences similar values of axial force and bending moment compared to  
703 the basic form-finding geometry (left). The application of i-MRA resulted in  
704 a decrease in the 6. Despite the geometric changes introduced, the imposed  
705 Von Mises stresses increased by less than 0.7 percent, which is a negligible  
706 increase. Moreover, the construction complexity of the work, as defined by  
707 the different types of structural elements used, was reduced by almost 10  
708 times.

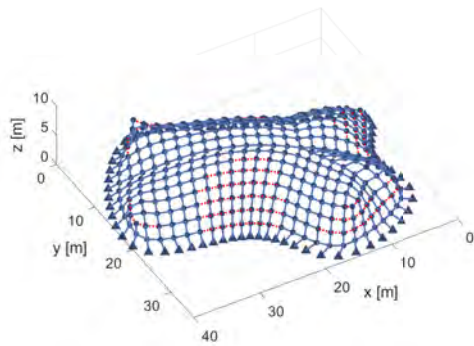
709 Finally, Figure 25*b* shows an interesting case of mesh composed of alter-  
710 nating hexagonal and pentagonal elements. This type of mesh is commonly  
711 used in geodesic dome design [45, 46, 47]. The advantage of this pattern  
712 lies in its ability to cover curved regular surfaces with geometrically regu-



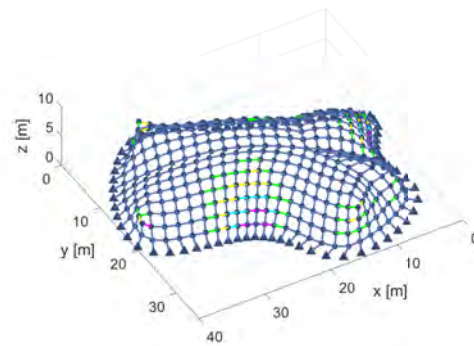
(a) MRA planimetric view



(b) i-MRA planimetric view



(c) MRA 3D view



(d) i-MRA 3D view

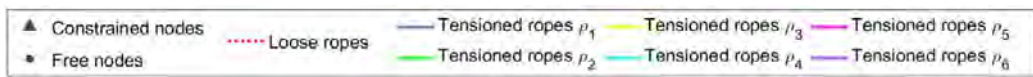


Figure 26: Comparison between MRA and i-MRA on a free-form structure with quadrangular mesh.

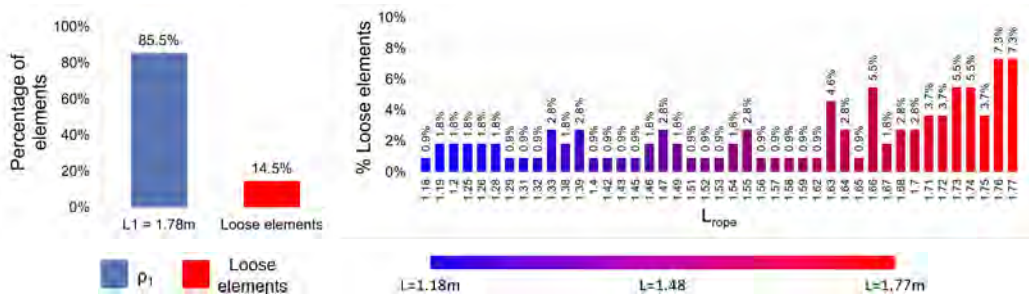


Figure 27: Application 4: Structural element lengths distribution applying the MRA.

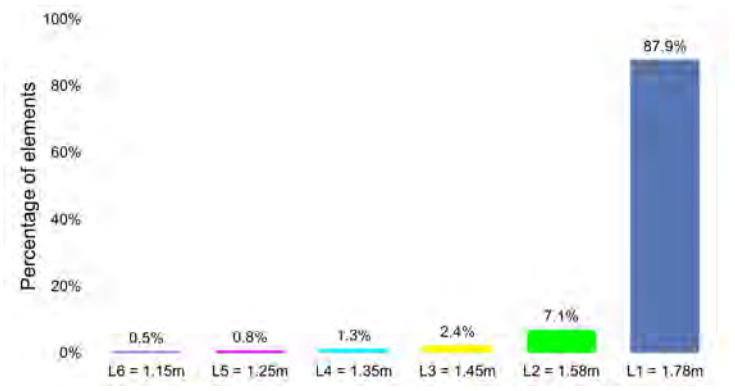


Figure 28: Application 4: Structural element lengths distribution applying the i-MRA.

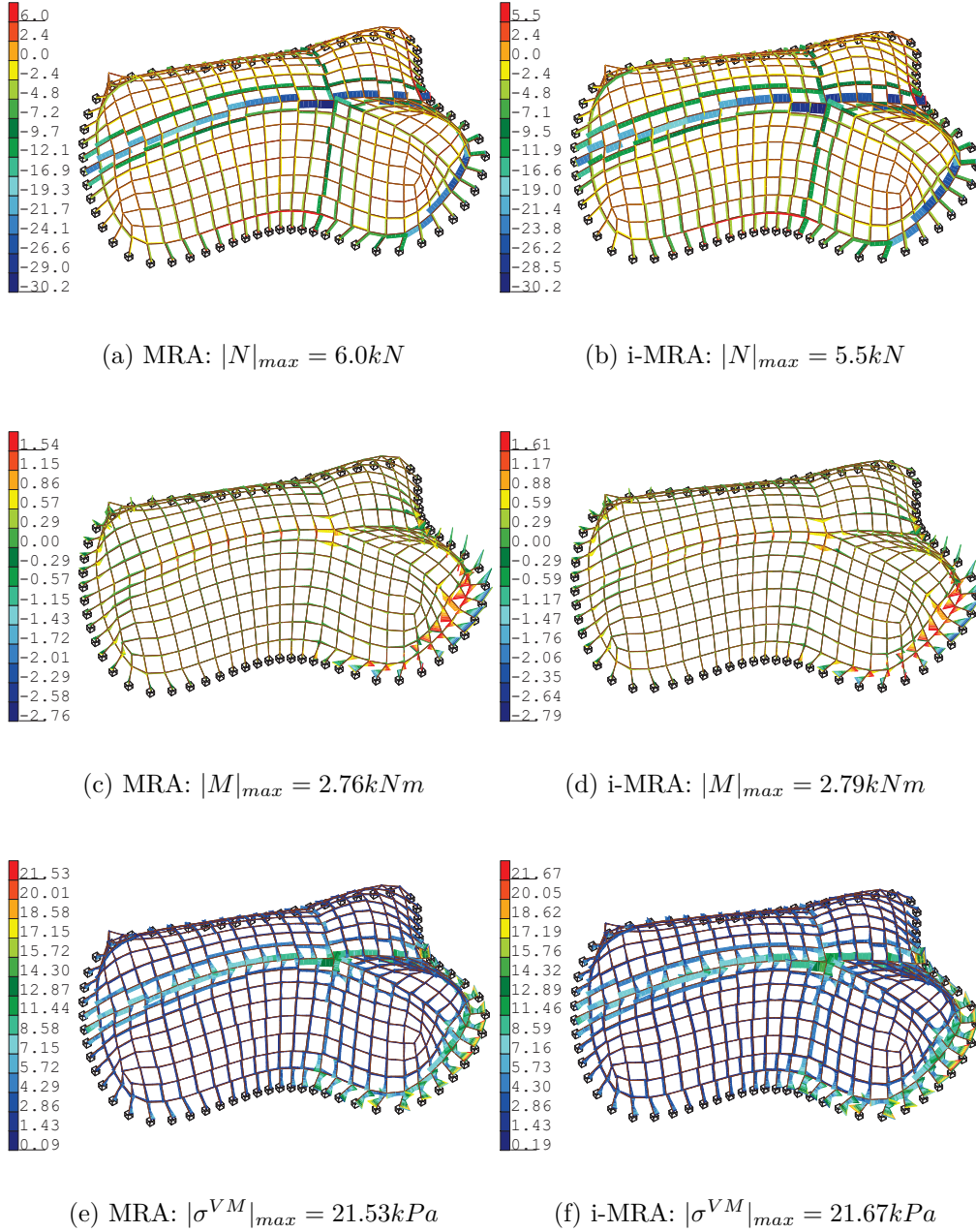


Figure 29: Structural analysis performed on the structures obtained by applying basic MRA (left) and i-MRA (right) on the application example with quadrangular mesh in Section 3.4. Comparison in terms of axial force [kN] (top), bending moment [kNm] (middle) and Von Mises stress [kPa] (bottom). 53

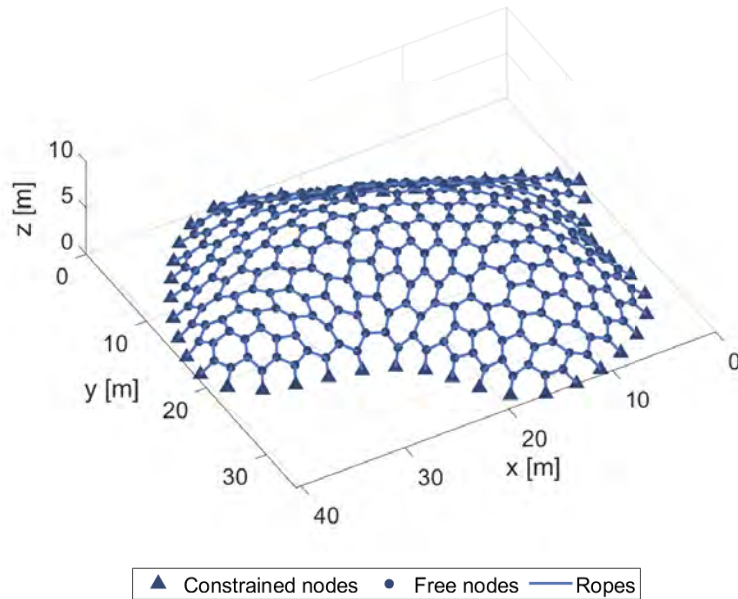


Figure 30: MRA application on a free-form structure with hexagonal mesh and  $\rho = 1.10$ .

713 lar planar elements. In fact, spherical domes are often designed using this  
 714 pattern.

715 In the presented example, the benefit of adopting this particular mesh  
 716 is related to the fact that each node is connected to a maximum of three  
 717 adjacent nodes. As a result, each node is constrained by a maximum of  
 718 three ropes, and the three degrees of freedom related to spatial translations  
 719 are tied by three ropes. This less restrictive system can evolve towards an  
 720 equilibrium configuration in which all the ropes composing the entire network  
 721 are tense. The direct outcome is that the geometry obtained by applying the  
 722 basic MRA is very shallow and consists of a single type of structural element,  
 723 as shown in Figure 30.

## 724 4. Conclusions

725 This paper presents a form-finding method that is specifically designed for  
726 gridshell structures. The method builds upon the Multi-body Rope Approach  
727 (MRA) developed by [29]. Once a load condition is defined, the basic MRA  
728 allows for the definition of the structural geometry that is characterized by  
729 the smaller eccentricity of applied compression forces. This helps to reduce  
730 bending moments and applied stress. The structure is modeled as a network  
731 of masses that are connected by loose ropes, and the solution of the dynamics  
732 of the system, subject to a specific load condition, allows the definition of a  
733 final equilibrium configuration that represents the structural geometry with  
734 the lowest bending moment.

735 To further minimize the complexity of structural construction manage-  
736 ment and reduce computational effort, two improvement techniques are pro-  
737 posed for the basic MRA. The first technique involves defining groups of  
738 structural elements with identical lengths, which helps to minimize the types  
739 of structural elements required for constructing the calculated structures.  
740 The second technique involves applying a repulsive force field to the dynamic  
741 model, which allows for tiny adjustments of the geometry to limit the num-  
742 ber of structural components that do not fit into the previously established  
743 groups. The combination of these two techniques is referred to as i-MRA.

744 The effectiveness of the proposed method was tested in four applica-  
745 tion examples of increasing complexity. The results showed that the i-MRA  
746 method leads to a significant reduction in the number of structural com-  
747 ponents required, especially as the geometric complexity of the structure  
748 increases.

749 The results of the structural analyses indicate that i-MRA induced changes  
750 on funicular structures calculated with basic MRA do not have significant  
751 impacts on their static behaviour. The increases observed in terms of inter-  
752 nal actions and stress were less than 1 % for almost all of the cases studied.  
753 Consequently, reducing the number of components analyzed has no adverse  
754 consequences from a structural perspective. However, it has important im-  
755 plications such as reducing production costs, encouraging mass production,  
756 and lowering expenses related to construction management.

757 The studied examples also demonstrated that the base mesh has no dis-  
758 cernible influence on the law connecting the slack coefficient to the structural  
759 height, which remains consistent in its qualitative trend.

760 However, the research also revealed that the initial mesh has a signif-  
761 icant impact on the final structural geometry. Thus, the selection of the  
762 basic mesh type is crucial. The research presented in this paper provides  
763 a foundation for further investigations on the subject, with potential future  
764 developments including an analysis of how the introduced methods may af-  
765 fect structural performance. Specifically, future research could investigate  
766 how the introduced geometric variations may impact the instability of the  
767 analyzed structures. Such an analysis could prove beneficial to both science  
768 and design practice.

769 Moreover, the proposed approach could be introduced into a structural  
770 optimization procedure, which could identify the optimal parameters for gen-  
771 erating the most effective structural shape while minimizing the costs asso-  
772 ciated with the projected structure. Finally, exploring and optimizing the  
773 optimal shapes for the panels and nodes that constitute the structure of the

774 gridshell could also represent an interesting research topic.

775     Indeed, while the methods presented in this paper can be helpful in  
776 achieving more efficient and cost-effective structures, the role of the designer  
777 remains critical. The designer’s knowledge and experience are essential in  
778 making informed decisions and balancing the trade-offs between structural  
779 performance, aesthetic appeal, and cost-effectiveness. The proposed methods  
780 should be seen as tools that can support the designer in the decision-making  
781 process, rather than a substitute for their expertise. It is through the col-  
782 laboration between the designer and the computational tools that the most  
783 optimal and effective design solutions can be achieved.

## 784 **5. Acknowledgments**

785     The authors acknowledge A. Brentegani for her contribution to the im-  
786 plementation of the Matlab codes for the method presented in this paper.

## 787 **References**

- 788 [1] J. N. Richardson, S. Adriaenssens, R. Filomeno Coelho, P. Bouillard, Coupled form-  
789 finding and grid optimization approach for single layer grid shells, *Engineering Struc-*  
790 *tures* 52 (2013) 230–239. doi:[https://doi.org/10.1016/j.engstruct.2013.02.](https://doi.org/10.1016/j.engstruct.2013.02.017)  
791 017.
- 792 [2] J. Chilton, C.-C. Chuang, Rooted in nature: aesthetics, geometry and structure in  
793 the shells of heinz isler, *Nexus Network Journal* 19 (3) (2017) 763–785. doi:<https://doi.org/10.1007/s00004-017-0357-5>.
- 794
- 795 [3] X. Tellier, Bundling elastic gridshells with alignable nets. part ii: Form-  
796 finding, *Automation in Construction* 141 (2022) 104292. doi:<https://doi.org/10.1016/j.autcon.2022.104292>.
- 797

- 798 URL [https://www.sciencedirect.com/science/article/pii/](https://www.sciencedirect.com/science/article/pii/S0926580522001650)  
799 S0926580522001650
- 800 [4] V. Tomei, E. Grande, M. Imbimbo, Design optimization of gridshells equipped  
801 with pre-tensioned rods, *Journal of Building Engineering* 52 (2022) 104407.  
802 doi:<https://doi.org/10.1016/j.jobe.2022.104407>.
- 803 URL [https://www.sciencedirect.com/science/article/pii/](https://www.sciencedirect.com/science/article/pii/S235271022200420X)  
804 S235271022200420X
- 805 [5] F. Otto, J. Hennieke, K. Matsushita, *Il10 gitterschalen*, Institut für leichte Flächen-  
806 tragwerke (IL)ISBN: 378282010X (1974).
- 807 [6] E. Happold, *Philosophy of design with particular respect to buildings*, London: E &  
808 FN Spon, 1997, ISBN: 9780429080012.
- 809 [7] B. Addis, D. Walker, *Happold: The confidence to build*, Taylor & Francis, 2005,  
810 ISBN: 9780203976487. doi:<https://doi.org/10.4324/9780203976487>.
- 811 [8] I. Liddell, *Frei otto and the development of gridshells*, *Case Studies in Structural*  
812 *Engineering* 4 (2015) 39–49. doi:<https://doi.org/10.1016/j.csse.2015.08.001>.
- 813 URL [https://www.sciencedirect.com/science/article/pii/](https://www.sciencedirect.com/science/article/pii/S2214399815300011)  
814 S2214399815300011
- 815 [9] W. Pan, M. Turrin, C. Louter, S. Sariyildiz, Y. Sun, Integrating multi-functional  
816 space and long-span structure in the early design stage of indoor sports arenas by us-  
817 ing parametric modelling and multi-objective optimization, *Journal of Building Engi-*  
818 *neering* 22 (2019) 464–485. doi:<https://doi.org/10.1016/j.jobe.2019.01.006>.
- 819 URL [https://www.sciencedirect.com/science/article/pii/](https://www.sciencedirect.com/science/article/pii/S2352710218304467)  
820 S2352710218304467
- 821 [10] W. Sobek, L. Blandini, *The mansueto library—notes on a glazed steel grid shell from*  
822 *design to construction*, in: *Challenging Glass Conference Proceedings*, Vol. 2, 2010,  
823 pp. 179–186. doi:<https://doi.org/10.7480/cgc.2.2316>.

- 824 [11] K. Fritzsche, W. van der Sluis, E. Smits, J. Bakker, Capital c, geometric optimization  
825 of a free-form steel gridshell towards planar quadrilateral glass units, in: Challenging  
826 Glass Conference Proceedings, Vol. 7, 2020. doi:[https://doi.org/10.7480/cgc.  
827 7.4493](https://doi.org/10.7480/cgc.7.4493).
- 828 [12] C. Zhao, J. Ma, S. Du, Y. Gu, Y. Zhou, Mechanical properties of a novel joint of a  
829 single-layer aluminum-alloy combined lattice-shell structure, *Materiali in tehnologije*  
830 53 (2019) 811–819. doi:<https://doi.org/10.1007/s12205-021-0239-y>.
- 831 [13] E. Happold, L. WI, Timber lattice roof for the mannheim bundesgartenschau, *The  
832 structural engineer* 53 (1975) 99–135.  
833 URL [https://docplayer.net/126675850-Timber-lattice-roof-for-the-mannheim-bundesgartenschau.  
834 html](https://docplayer.net/126675850-Timber-lattice-roof-for-the-mannheim-bundesgartenschau.html)
- 835 [14] R. Harris, Design of timber gridded shell structures, *Proceedings of the Institution  
836 of Civil Engineers - Structures and Buildings* 164 (2) (2011) 105–116. doi:[10.1680/  
837 stbu.9.00088](https://doi.org/10.1680/stbu.9.00088).
- 838 [15] M. Collins, T. Cosgrove, A review of the state of the art of timber gridshell design  
839 and construction, in: *Civil Engineering Research in Ireland CERI 2016 Conference  
840 Proceeding*, Civil Engineering Research Association of Ireland CERAI, 2016.  
841 URL <https://hdl.handle.net/10344/5192>
- 842 [16] J. Chilton, G. Tang, *Timber gridshells: architecture, structure and craft*, Routledge,  
843 2016, ISBN: 9781138775305. doi:<https://doi.org/10.4324/97811315773872>.
- 844 [17] C. Douthe, J. Caron, O. Baverel, Gridshell structures in glass fibre reinforced  
845 polymers, *Construction and Building Materials* 24 (9) (2010) 1580–1589.  
846 doi:<https://doi.org/10.1016/j.conbuildmat.2010.02.037>.  
847 URL [https://www.sciencedirect.com/science/article/pii/  
848 S0950061810000802](https://www.sciencedirect.com/science/article/pii/S0950061810000802)
- 849 [18] F. T. Olivier Baverel, Jean-François Caron, L. D. Peloux, Gridshells in com-  
850 posite materials: Construction of a 300 m2 forum for the solidays' festival in

- 851 paris, *Structural Engineering International* 22 (3) (2012) 408–414. doi:10.2749/  
852 101686612X13363869853572.
- 853 [19] B. D’Amico, A. Kermani, H. Zhang, A. Pugnale, S. Colabella, S. Pone, Timber grid-  
854 shells: Numerical simulation, design and construction of a full scale structure, *Struc-*  
855 *tures* 3 (2015) 227–235. doi:<https://doi.org/10.1016/j.istruc.2015.05.002>.  
856 URL [https://www.sciencedirect.com/science/article/pii/  
857 S2352012415000557](https://www.sciencedirect.com/science/article/pii/S2352012415000557)
- 858 [20] M. Bagneris, R. Motro, B. Maurin, N. Pauli, Structural morphology issues in con-  
859 ceptual design of double curved systems, *International Journal of Space Structures*  
860 23 (2) (2008) 79–87. doi:10.1260/026635108785260560.
- 861 [21] E. L. Hernández, O. Baverel, C. Gengnagel, On the design and construction of elastic  
862 gridshells with irregular meshes, *International Journal of Space Structures* 28 (3-4)  
863 (2013) 161–174. doi:10.1260/0266-3511.28.3-4.161.
- 864 [22] S. H. Dyvik, B. Manum, A. Rønquist, Gridshells in recent research—a systematic  
865 mapping study, *Applied Sciences* 11 (24) (2021). doi:10.3390/app112411731.  
866 URL <https://www.mdpi.com/2076-3417/11/24/11731>
- 867 [23] L. Gründig, E. Moncrieff, P. Singer, D. Ströbel, A history of the principal devel-  
868 opments and applications of the force density method in germany 1970–1999, in:  
869 *Proceedings of IASS-IACM 2000 Fourth International Colloquium on Computation*  
870 *of Shell & Spatial Structures*, Chania-Crete, Greece, 2000.  
871 URL [https://www.technet-gmbh.com/fileadmin/user\\_upload/technet/  
872 Publikationen/Easy/Density2.pdf](https://www.technet-gmbh.com/fileadmin/user_upload/technet/Publikationen/Easy/Density2.pdf)
- 873 [24] R. Mesnil, C. Douthe, O. Baverel, T. Gobin, Form finding of nexorades us-  
874 ing the translations method, *Automation in Construction* 95 (2018) 142–154.  
875 doi:<https://doi.org/10.1016/j.autcon.2018.08.010>.  
876 URL [https://www.sciencedirect.com/science/article/pii/  
877 S092658051830147X](https://www.sciencedirect.com/science/article/pii/S092658051830147X)

- 878 [25] H.-J. Schek, The force density method for form finding and computation of general  
879 networks, *Computer Methods in Applied Mechanics and Engineering* 3 (1) (1974)  
880 115–134. doi:[https://doi.org/10.1016/0045-7825\(74\)90045-0](https://doi.org/10.1016/0045-7825(74)90045-0).  
881 URL [https://www.sciencedirect.com/science/article/pii/  
882 0045782574900450](https://www.sciencedirect.com/science/article/pii/S0045782574900450)
- 883 [26] J. R. H. OTTER, A. C. CASSELL, R. E. a. HOBBS, Dynamic relaxation, *Proceedings*  
884 *of the Institution of Civil Engineers* 35 (4) (1966) 633–656. doi:10.1680/iicep.  
885 1966.8604.
- 886 [27] P. Block, J. Ochsendorf, Thrust network analysis: A new methodology for three-  
887 dimensional equilibrium, *Journal of the International Association for Shell and*  
888 *Spatial Structures* 48 (3) (2007) 167–173.  
889 URL [https://www.ingentaconnect.com/content/iass/jiass/2007/00000048/  
890 00000003/art00011](https://www.ingentaconnect.com/content/iass/jiass/2007/00000048/00000003/art00011)
- 891 [28] A. Kilian, J. Ochsendorf, Particle-spring systems for structural form finding, *Journal*  
892 *of the International Association for Shell and Spatial Structures* 46 (2) (2005) 77–84.  
893 URL [https://www.ingentaconnect.com/content/iass/jiass/2005/00000046/  
894 00000002/art00003](https://www.ingentaconnect.com/content/iass/jiass/2005/00000046/00000002/art00003)
- 895 [29] A. Manuello, Multi-body rope approach for grid shells: Form-finding  
896 and imperfection sensitivity, *Engineering Structures* 221 (2020) 111029.  
897 doi:<https://doi.org/10.1016/j.engstruct.2020.111029>.  
898 URL [https://www.sciencedirect.com/science/article/pii/  
899 S0141029620309895](https://www.sciencedirect.com/science/article/pii/S0141029620309895)
- 900 [30] I. M. Rian, M. Sassone, S. Asayama, From fractal geometry to architecture: Design-  
901 ing a grid-shell-like structure using the takagi–landsberg surface, *Computer-Aided*  
902 *Design* 98 (2018) 40–53. doi:<https://doi.org/10.1016/j.cad.2018.01.004>.  
903 URL [https://www.sciencedirect.com/science/article/pii/  
904 S0010448518300423](https://www.sciencedirect.com/science/article/pii/S0010448518300423)

- 905 [31] Z. Zhao, D. Yu, T. Zhang, N. Zhang, H. Liu, B. Liang, L. Xian, Ef-  
906 ficient form-finding algorithm for freeform grid structures based on in-  
907 verse hanging method, *Journal of Building Engineering* 46 (2022) 103746.  
908 doi:<https://doi.org/10.1016/j.jobe.2021.103746>.  
909 URL [https://www.sciencedirect.com/science/article/pii/](https://www.sciencedirect.com/science/article/pii/S2352710221016041)  
910 [S2352710221016041](https://www.sciencedirect.com/science/article/pii/S2352710221016041)
- 911 [32] W. Huang, C. Wu, J. Hu, W. Gao, Weaving structure: A bending-active grid-  
912 shell for freeform fabrication, *Automation in Construction* 136 (2022) 104184.  
913 doi:<https://doi.org/10.1016/j.autcon.2022.104184>.  
914 URL [https://www.sciencedirect.com/science/article/pii/](https://www.sciencedirect.com/science/article/pii/S0926580522000577)  
915 [S0926580522000577](https://www.sciencedirect.com/science/article/pii/S0926580522000577)
- 916 [33] K. Yamamoto, T. Ogawa, M. Fujimoto, C. Lazaro, T. Takeuchi, S.-D. Xue, P.-S.  
917 Chen, S. Kato, State-of-the-art for optimization of forms and strength for reticulated  
918 shells, in: *International Association for Shell and Spatial Structures 2012: From*  
919 *Spatial Structures to Space Structures*, 2012.
- 920 [34] S. Adriaenssens, P. Block, D. Veenendaal, C. Williams, *Shell structures for archi-*  
921 *tecture: form finding and optimization*, Routledge, 2014, ISBN: 9780415840606.  
922 doi:<https://doi.org/10.4324/9781315849270>.
- 923 [35] L. Bouhaya, O. Baverel, J.-F. Caron, Optimization of gridshell bar orientation using a  
924 simplified genetic approach, *Structural and Multidisciplinary Optimization* 50 (2014)  
925 839–848. doi:<https://doi.org/10.1007/s00158-014-1088-9>.
- 926 [36] C. Douthe, R. Mesnil, H. Orts, O. Baverel, Isoradial meshes: Covering elastic  
927 gridshells with planar facets, *Automation in Construction* 83 (2017) 222–236.  
928 doi:<https://doi.org/10.1016/j.autcon.2017.08.015>.  
929 URL [https://www.sciencedirect.com/science/article/pii/](https://www.sciencedirect.com/science/article/pii/S0926580517307367)  
930 [S0926580517307367](https://www.sciencedirect.com/science/article/pii/S0926580517307367)
- 931 [37] N. Montagne, C. Douthe, X. Tellier, C. Fivet, O. Baverel, Discrete voss surfaces:  
932 Designing geodesic gridshells with planar cladding panels, *Automation in Construc-*

- 933 tion 140 (2022) 104200. doi:<https://doi.org/10.1016/j.autcon.2022.104200>.  
934 URL [https://www.sciencedirect.com/science/article/pii/  
935 S0926580522000735](https://www.sciencedirect.com/science/article/pii/S0926580522000735)
- 936 [38] H. Seifi, A. Rezaee Javan, S. Xu, Y. Zhao, Y. M. Xie, Design optimization and  
937 additive manufacturing of nodes in gridshell structures, *Engineering Structures* 160  
938 (2018) 161–170. doi:<https://doi.org/10.1016/j.engstruct.2018.01.036>.  
939 URL [https://www.sciencedirect.com/science/article/pii/  
940 S0141029617320564](https://www.sciencedirect.com/science/article/pii/S0141029617320564)
- 941 [39] I. M. de Oliveira, R. M. de Oliveira Pauletti, L. C. Meneghetti, Connec-  
942 tion system for gridshell structures using parametric modeling and digital  
943 fabrication, *Automation in Construction* 109 (2020) 102996. doi:<https://doi.org/10.1016/j.autcon.2019.102996>.  
944 URL [https://www.sciencedirect.com/science/article/pii/  
945 S0926580519306612](https://www.sciencedirect.com/science/article/pii/S0926580519306612)
- 947 [40] A. M. Bertetto, F. Riberi, Form-finding of pierced vaults and digital fabrication of  
948 scaled prototype, *Curved and Layered Structures* 8 (1) (2021) 210–224 [cited 2023-  
949 11-08]. doi:[doi:10.1515/cls-2021-0020](https://doi.org/10.1515/cls-2021-0020).  
950 URL <https://doi.org/10.1515/cls-2021-0020>
- 951 [41] A. Manuello Bertetto, J. Melchiorre, L. Sardone, G. Marano, et al., Multi-body rope  
952 approach for the form-finding of shape optimized grid shell structures, in: *Pursuing  
953 the Infinite Potential of Computational Mechanics*, International Centre for Numerical  
954 Methods in Engineering, CIMNE, 2022. doi:[10.23967/wccm-apcom.2022.075](https://doi.org/10.23967/wccm-apcom.2022.075).
- 955 [42] SOFiSTiK, Text Editor 2023, Flataustr. 14, 90411 Nuremberg, 2022.  
956 URL <https://www.sofistik.com>(lastvisited:8November2023)
- 957 [43] J. Melchiorre, S. Soutiropoulos, A. Manuello Bertetto, G. C. Marano, F. Marmo,  
958 Grid-shell multi-step structural optimization with improved multi-body rope ap-  
959 proach and multi-objective genetic algorithm, in: S. Gabriele, A. Manuello Bertetto,

- 960 F. Marmo, A. Micheletti (Eds.), *Shell and Spatial Structures*, Springer Na-  
961 ture Switzerland, Cham, 2024, pp. 62–72. doi:[https://doi.org/10.1007/](https://doi.org/10.1007/978-3-031-44328-2_7)  
962 [978-3-031-44328-2\\_7](https://doi.org/10.1007/978-3-031-44328-2_7).
- 963 [44] MATLAB, version (R2022b) access (8 November 2023), The MathWorks Inc., Natick,  
964 Massachusetts, 2022.  
965 URL <https://www.mathworks.com/products/matlab.html>
- 966 [45] T. Tarnai, Geodesic domes and fullerenes, *Philosophical Transactions of the Royal*  
967 *Society of London. Series A: Physical and Engineering Sciences* 343 (1667) (1993)  
968 145–154. doi:<https://doi.org/10.1098/rsta.1993.0048>.
- 969 [46] G. Pavlov, Geodesic domes bounded by symmetrical mainly hexagonal elements,  
970 *International Journal of Space Structures* 9 (2) (1994) 53–66. doi:[10.1177/](https://doi.org/10.1177/026635119400900201)  
971 [026635119400900201](https://doi.org/10.1177/026635119400900201).
- 972 [47] H. Miura, M. Kimoto, A comparison of grid quality of optimized spherical hexagonal–  
973 pentagonal geodesic grids, *Monthly Weather Review* 133 (10) (2005) 2817 – 2833.  
974 doi:<https://doi.org/10.1175/MWR2991.1>.  
975 URL [https://journals.ametsoc.org/view/journals/mwre/133/10/mwr2991.1.](https://journals.ametsoc.org/view/journals/mwre/133/10/mwr2991.1.xml)  
976 [xml](https://journals.ametsoc.org/view/journals/mwre/133/10/mwr2991.1.xml)